International Journal of Remote Sensing

ISSN: (Print) (Online) Journal homepage: https://www.tandfonline.com/loi/tres20

Accuracy of satellite-derived solar direct irradiance in Southern Spain and Switzerland

Laurent Vuilleumier , Angela Meyer , Reto Stöckli , Stefan Wilbert & Luis F. Zarzalejo

To cite this article: Laurent Vuilleumier , Angela Meyer , Reto Stöckli , Stefan Wilbert & Luis F. Zarzalejo (2020) Accuracy of satellite-derived solar direct irradiance in Southern Spain and Switzerland, International Journal of Remote Sensing, 41:22, 8808-8838, DOI: 10.1080/01431161.2020.1783712

To link to this article: https://doi.org/10.1080/01431161.2020.1783712

Published online: 09 Sep 2020.

INTERNATIONAL JOURNAL OF REMOTE SENSING
2020, VOL. 41, NO. 22, 8808–8838
https://doi.org/10.1080/01431161.2020.1783712

Taylor & Francis
Taylor & Francis Group

Accuracy of satellite-derived solar direct irradiance in Southern Spain and Switzerland

Laurent Vuilleumier[a*], Angela Meyer[a*], Reto Stöckli[b], Stefan Wilbert[c] and Luis F. Zarzalejo[d]

[a]Measurement and Data Department, Federal Office of Meteorology and Climatology MeteoSwiss, Payerne, Switzerland; [b]Analysis and Forecast Department, Federal Office of Meteorology and Climatology MeteoSwiss, Zurich, Switzerland; [c]Institute of Solar Research, German Aerospace Centre, Tabernas, Spain; [d]Renewable Energy Division, Centre for Energy, Environment and Technological Research CIEMAT, Madrid, Spain

ABSTRACT

We present a validation study of direct normal irradiance (DNI) estimates from HelioMont with ground-based measurements from two European sites for the year 2015. The HelioMont algorithm infers irradiance with data from the Meteosat Second Generation Spinning Enhanced Visible and Infrared Imager (SEVIRI) instrument as the primary source of information on clouds, and data from models or reanalysis for other influential input parameters. The validation sites are the Plataforma Solar de Almería (PSA), a solar power research facility in Southern Spain characterized by arid conditions and the Swiss Baseline Surface Radiation Network (BSRN) site of Payerne, characterized by a much more frequent cloud coverage. Our analysis shows the importance of separately evaluating the quality of (1) the clear-sky irradiance computation and (2) the determination of the cloud effect. We also specifically investigate the cloud modification factor (CMF) using a validation CMF derived from ground-based data, giving us more insight into event-by-event agreement between HelioMont estimates and measured irradiances. The clear-sky HelioMont DNI uncertainty is mainly influenced by the aerosol optical depth (AOD) input data. Using the original AOD input (a 2008 climatology based on data from the Aerosol Comparisons between Observations and Models project) leads to large negative biases of 115 W m^{-2} to 145 W m^{-2}. Using AOD from the Copernicus Atmosphere Monitoring Service (CAMS) allows reducing these biases to 15 W m^{-2} to 25 W m^{-2} (2% to 3%) with a dispersion of ±12% to ±15%, which is the HelioMont clear-sky DNI expanded uncertainty when using CAMS AOD. Using ground-measured AOD reduces this uncertainty to ±5% to ±6.5%, which is probably the limit of what is achievable with HelioMont. For all-sky comparisons, mean biases were between about −5 W m^{-2} and 55 W m^{-2} (depending on AOD input and station), while the root-mean-square deviation (RMSD) was between about 175 W m^{-2} and 195 W m^{-2}. Our validation method yielded

ARTICLE HISTORY
Received 8 November 2019
Accepted 12 May 2020

CONTACT Laurent Vuilleumier laurent.vuilleumier@meteoswiss.ch Measurement and Data Department, Federal Office of Meteorology and Climatology MeteoSwiss,, Payerne CH-1530, Switzerland

*These authors contributed equally to this work.

correlation between HelioMont and validation CMF between 0.79 and 0.92 (Pearson's correlation coefficient *r*), while RMSD was between 0.18 and 0.24. The computation of the cloud effect is the part of HelioMont that is the main source of uncertainty. Systematic errors were identified (underestimation of the number of near-zero DNI and overestimation of the number of clear-sky cases) and solving them may lead to substantial improvement.

1. Introduction

An accurate retrieval of surface solar irradiance from satellite measurements is key to a large number of atmospheric observations and modelling studies, including climate monitoring and climate model validation efforts (e.g. Posselt et al. 2012). Satellite-retrieved surface solar irradiance also plays an important role in solar energy applications, for example, for estimating the solar resource potential of a particular region or site. A reliable prediction of the direct normal irradiance (DNI) component, in particular on short time scales of minutes to hours, is particularly relevant at large-concentrated solar power plants, as it facilitates a more efficient operation of such plants (Nouri et al. 2019). Accurate retrieval of surface DNI from satellite measurements is also key in DNI now-casting at hourly timescales (Schroedter-Homscheidt and Wilbert 2017).

Clouds are the most important source of DNI variability at the Earth's surface. Stratus clouds can reduce DNI to zero for hours and days, while shallow cumulus clouds usually induce high temporal and spatial variability in surface DNI. Thin cirrus clouds may cause lower reductions of surface DNI and still somewhat elevated DNI variability. Atmospheric aerosol particles are the second most important source of surface DNI variability. Strong mineral dust outbreaks can increase the atmospheric aerosol optical depth (AOD) to more than 1 and thereby reduce the DNI by 40% and more. Over Southern Europe, the strongest AOD increases are usually observed after mineral dust outbreaks and transport from the Saharan desert. Saharan dust events can clearly have a short-term impact on the production of solar energy (Slingo et al. 2006).

In this study, the HelioMont algorithm (Stöckli 2013) relying on input data from satellite platforms and other sources was used to infer the surface DNI for two European sites performing high-quality DNI ground-based measurements, which were then used to validate the satellite-derived irradiance. HelioMont is part of the Heliosat algorithm family (e.g. Moeser and Raschke 1984; Cano et al. 1986; Mueller et al. 2004; Posselt et al. 2012, 2014). Strictly speaking, the HelioMont algorithm relies on purely satellite-derived data only for determining the effect of clouds on radiation. However, we follow a common practice of other studies (Amillo, Huld and Müller, 2014; Bright 2019; Damiani et al. 2018; Federico et al. 2017; Greuell, Meirink, and Wang 2013; Mueller et al. 2009; Perez et al. 2002; Porfirio and Ceballos 2017) in describing our dataset as satellite-derived even though the input data are not all obtained solely from satellite platforms.

The validation sites are the Plataforma Solar de Almería (PSA, 37.1° N, 2.36° W) and the Swiss station of the Baseline Surface Radiation Network (BSRN [Ohmura et al., 1998]) at Payerne (PAY, 46.8° N, 6.94° E). The PSA is a solar power research facility belonging to the Spanish Centre for Energy, Environment and Technological Research (CIEMAT). The PSA

site covers an area of about 1 km^2, and is equipped with dozens of high-quality shortwave radiometers, including sun-tracker mounted pyrheliometers monitoring DNI. This site is about the same size as the horizontal pixel resolution of the Meteosat Second Generation (MSG) Spinning Enhanced Visible and Infrared Imager (SEVIRI) visible channel, which is predominantly used by the HelioMont algorithm for cloud detection, and that makes it an ideal validation site for HelioMont. If only a single in situ instrument is used, a point measurement of DNI would be compared to an effective DNI average taken over the pixel area. Ground-based DNI derived from multiple instruments is more representative of the area average (see [Huang et al. 2016] for global horizontal irradiance). Moreover, only the use of multiple in situ instruments can provide us with an estimate of the sub-grid spatial variability, which in turn gives us a measure of the agreement to expect between satellite-derived and in situ measured DNIs.

The Payerne station (PAY) is one of about 55 active BSRN radiation-monitoring sites. At PAY, DNI is monitored with a single pyrheliometer, which thus does not provide the same possibility of sampling a complete SEVIRI pixel as at PSA. However, it is of interest to compare the results from PSA and PAY, since at PSA, there is a predominance of clear-sky or at least fair weather situations, while at PAY cloudy situations are predominant.

Other studies presented validation of irradiance dataset derived using information from satellite (especially information on cloud properties) and other sources. To assess the agreement between the satellite estimates and the validation ground-based measurements, statistical indicators aggregating the differences between the satellite estimates and the corresponding ground-based measurements, such as mean biases, mean absolute biases (MAB), root-mean-square deviation (RMSD), correlation coefficient, etc., were used. DNI satellite-derived estimates were compared to corresponding ground-based measurements in the following studies (Amillo, Huld and Müller, 2014; Castelli et al. 2014; Eissa et al. 2015; Greuell, Meirink, and Wang 2013; Mueller and Traeger-Chatterjee 2014; Perez et al. 2002; Porfirio and Ceballos 2017). Similarly, global horizontal irradiance (GHI) satellite estimates were also validated in many studies (Amillo, Huld and Müller, 2014; Bright 2019; Damiani et al. 2018; Eissa et al. 2015; Federico et al. 2017; Greuell, Meirink, and Wang 2013; Kosmopoulos et al. 2018; Perez et al. 2002). While the set of statistical indicators used varies depending on the study, almost all studies provide at least mean biases and RMSD. We also use these indicators, which allows a comparison of our results with these studies. However, we also aim at demonstrating that an analysis going beyond such statistical indicators can reveal errors or inaccuracies in the irradiance estimation algorithm that would be very difficult to identify otherwise. In particular, we analyse the cloud modification factor (CMF), which is a ratio from a normalization of the all-sky estimate or measurement with the corresponding clear-sky theoretical estimate.

The objective of our study is to assess the accuracy of the MSG-derived clear-sky and all-sky DNI by comparison to the in situ measured DNIs, and to identify and eventually explain potential discrepancies in the MSG-derived DNI. We performed this study as part of the Direct Normal Irradiance Nowcasting (DNICast, 2020) project of the European Union's Seventh Programme for research, technological development and demonstration framework, hence our focus on the DNI component. The DNICast project made available a one-year dataset (year 2015) with DNI measured by multiple pyrheliometers at PSA. At PSA and PAY, other ground-based irradiance measurements (global and diffuse horizontal irradiance) further enhance data quality control and are also used to identify clear-sky

times. This allows a specific clear-sky validation, as well as a subsequent CMF analysis of discrepancies that are related to the representation of the cloud effect in the HelioMont algorithm.

Our study is, to the best of our knowledge, the first study to validate Meteosat-derived DNI by a multiplicity of pyrheliometers rather than a single instrument. We could not find in all the studies cited above, examples of multiple instruments used on the same site. We found only two investigation of model-derived surface irradiance using multiple ground sensors in relatively close vicinity (Huang et al. 2016; Li et al. 2005). In both cases, the studies investigated GHI and the goal of these studies was not the validation of the estimated dataset. It was the determination of the sampling error due to spatial variability when comparing point ground surface measurements to area averages. We also add to previous studies by testing different sources for AOD data to investigate how they influence the accuracy of clear-sky estimations by an algorithm of the Heliosat-family.

2. Data and methods

2.1. HelioMont retrieval of DNI

Irradiances, including DNI, were derived at 15 minute intervals for the PSA and PAY sites using HelioMont. This algorithm calculates surface solar irradiance and its components like horizontal direct beam and diffuse irradiance as well as DNI with a combination of a radiative-transfer-model-based clear-sky and a satellite-based cloud-forcing algorithm.

The cloud forcing follows the classical Heliosat approach (Moeser and Raschke 1984; Cano et al. 1986; Mueller et al. 2004; Posselt et al. 2012, 2014) where satellite measured reflectances are contrasted to cloud-free (surface) reflectances to estimate radiative cloud forcing. HelioMont additionally employs near-infrared and infrared channels over bright targets (where visual contrast between clouds and the underlying surface would not be sufficient). Specifically, it employs the MSG-SEVIRI High-Resolution Visible (HRV; 0.45 µm to 1.10 µm) channel in combination with five other near-infrared and infrared channels (0.6, 0.8, 1.6, 10.8, 12.0 µm).

The primary step to get a satellite-based cloud forcing is to know the clear-sky state of the observed target. This is achieved by collecting cloud-screened visible and infrared observations from the last days (up to 10 days), and weighting observations by age and cloud screening uncertainty. With geostationary satellite data covering the full diurnal cycle, missing observations can be overcome by inverting the diurnal cycle of clear-sky reflectance and brightness temperature using parametric reflectance and temperature models (see chapter 6 of [Stöckli 2013]).

The next step is to contrast the actual (all-sky) reflectance and brightness temperature with the above retrieved clear-sky state. In the classical Heliosat approach, this yields a so-called cloud index (CI), which is a normalized difference of all-sky minus clear-sky reflectance. CI is around 0 for clear-sky and around 1 for completely cloudy scenes (see chapter 8.2 of [Stöckli 2013]). This method fails for bright surface targets where the clear-sky can have a similar or even higher reflectance as the all-sky. In HelioMont we thus employ near-infrared (0.8, 1.6 µm) and thermal-infrared (10.8 and 12.0 µm) channels to generate CI for clear-sky reflectance above 0.5 (see chapter 8.3 and 8.4 of [Stöckli 2013]). From CI the clear-sky index (K) is calculated by the use of a parametric formula trained with station

data (see chapter 8.5 of [Stöckli 2013]). It also includes topographic effects on surface solar irradiance. The (satellite-observed) K is multiplied with the radiative transfer modelled clear-sky irradiance to get the all-sky irradiance. It thus exactly corresponds to the CMF formulation used in station data where CMF is defined as all-sky irradiance divided by (theoretical, modelled) clear-sky irradiance.

The clear-sky irradiance is not derived from satellite observations, but with an algorithm using input data from models or reanalyses. However, as indicated below satellite data assimilation is key in ensuring the accuracy of these input data. The clear-sky algorithm is based on look-up tables that have been built using the radiative transfer model libRadtran (Mayer and Kylling 2005). The look-up tables reflect the effects of the atmospheric conditions (water vapour, ozone, and aerosol) on solar radiative fluxes. European Centre for Medium-Range Weather Forecasts (ECMWF) European Reanalysis (ERA) Interim archive (Berrisford et al. 2009) was used to prescribe the total column water vapour and ozone forcing. In the ERA-Interim analysis, satellite data assimilation is used for correcting bias and ensuring good agreement between ERA-Interim products and observations. In particular, the total precipitable water is used as one of the bias predictors in ERA-Interim variational bias correction scheme based on satellite radiance assimilation (Dee and Uppala 2009).

The AOD at 550 nm characterizes the aerosol load using a default aerosol mix. Originally, HelioMont used a climatology of AOD at 550 nm from Kinne (2008) that was derived using AOD data from the Aerosol Comparisons between Observations and Models (AeroCom) project (Kinne et al. 2006) and from the AErosol RObotic NETwork (AERONET). In our analysis, we used HelioMont DNI estimates based on the original Kinne AOD climatology as well as two other DNI datasets from HelioMont reruns, the first using AOD data from the Copernicus Atmosphere Monitoring Service (CAMS [Inness et al. 2013]), and the second using AOD measurements from sun photometers located near the sites. The treatment of AOD, the AOD sun photometer measurements, and the CAMS dataset are described in more detailed below in the subsection describing aerosol optical properties.

2.2. *In situ measured irradiances*

After assessing PSA DNI pyrheliometer measurements from January to December 2015, we selected for analysis the data from the four PSA pyrheliometers listed in Table 1. The

Table 1. List of pyrheliometers used for the HelioMont validation at PSA. There are 7603 (43.2%) valid and simultaneous daytime DNI measurements of all four instruments during SEVIRI scanning of PSA in 2015.

Station name	Instrument type	Position longitude, latitude (°W, °N)	Operator	Number of valid daytime DNI measurements during SEVIRI scanning of PSA in 2015	Percentage value (%)
DISS	K&Z CHP1	2.359646, 37.097722	CIEMAT	15,423	87.7
PSA-HP	K&Z CHP1	2.358106, 37.090876	DLR	14,754	83.9
CESA-NORTE	Eppley NIP	2.361192, 37.098649	CIEMAT	11,352	64.6
CESA-SUR	Eppley NIP	2.361265, 37.094824	DLR	13,710	78.0

instruments are thermopile-based and mounted on sun trackers. Their positions, indicated in Figure 1(a), are well scattered across the PSA site, which makes the four in situ measured DNIs approximately representative of the entire site. Two of the pyrheliometers are of Kipp & Zonen (K&Z) CHP1 type; the other two are of type Eppley NIP. The number of valid measurements is provided in Table 1 for each instrument. Figure 1(b) shows the availability of valid DNI measurements from the pyrheliometers in 2015. Data from two other pyrheliometers were excluded from our analysis because of low data availability. The one at the PSA station CESA1 had a comparatively low number of valid DNI values in 2015, due to irregularities in its cleaning schedule from January to May 2015. Likewise, no valid METAS DNI data were available for August to December 2015.

All DNI measurements were subjected to automatic quality control (QC) in accordance with the Long and Dutton (2010) QC test recommendations for the BSRN. The data from PSA-HP were also tested according to (Geuder et al. 2015). In addition, all data sets were visually inspected to remove remaining artefacts arising from shadowing. This QC procedure ensured that the DNI measurements used in our study are of a quality similar to what Vuilleumier et al. (2014) estimated for DNI at PAY when an absolute cavity radiometer is not permanently used for on-line calibration. This corresponds to an expanded uncertainty of about 1.6%. The in situ DNIs are 1-minute averages of 1 Hz sampling, whereas the HelioMont algorithm uses input data from various sources with different temporal and spatial granularity. Among these, the parameter with the highest spatial and temporal variability is the cloud effect that is estimated using SEVIRI radiance measurements taken during less than one microsecond every 15 minutes while scanning the pixels corresponding to each of our two sites. For comparisons, we have used three subsets derived from our in situ DNI data:

(1) the 1 minute in situ measurement corresponding to the time of SEVIRI scan (rounded to the minute),
(2) 15 minute-averages of in situ measurements centred on the time of SEVIRI scan,
(3) 1-hour averages of in situ measurements (from minute 00 to 59) to be compared with 1-hour averages of HelioMont data (4 scans).

We used two validation strategies at PSA, the first maximizing data time availability, the second maximizing spatial representativity. The first approach used all data times when at least one of the four pyrheliometer provided valid data in one combined data set: PSA-HP DNI was used as default and DISS DNI was used whenever valid PSA-HP DNI data were unavailable. This approach achieved 98% availability of valid (circumsolar ratio-corrected – CSR-corrected – see the following subsection) DNI data at solar zenith angles less than 90°. Such a high data availability ensured that all seasons were equally represented in our dataset. Our second approach used only data when all four pyrheliometers had valid measurements. This approach is more spatially representative because it uses the average of the four DNIs measured at different locations on the PSA site ('SrfCmb,' see Figure 1(b)). But it is not entirely representative in a climatological sense because it includes only 43% of DNI data at solar zenith angles less than 90°, and it specially contains few DNI values for April and August 2015 (underrepresented months). Combining the two approaches allows us using the more spatially representative dataset, while verifying with


(a)
CESA-Norte
DISS
CESA-Sur
PSA-HP
N
1 km
© 2018 Google
Google earth
Bildaufnahmedatum: 9/4/2017 Breite 37.090486° Lange -2.370090° Höhe 484 m sichthohe 2.06 km

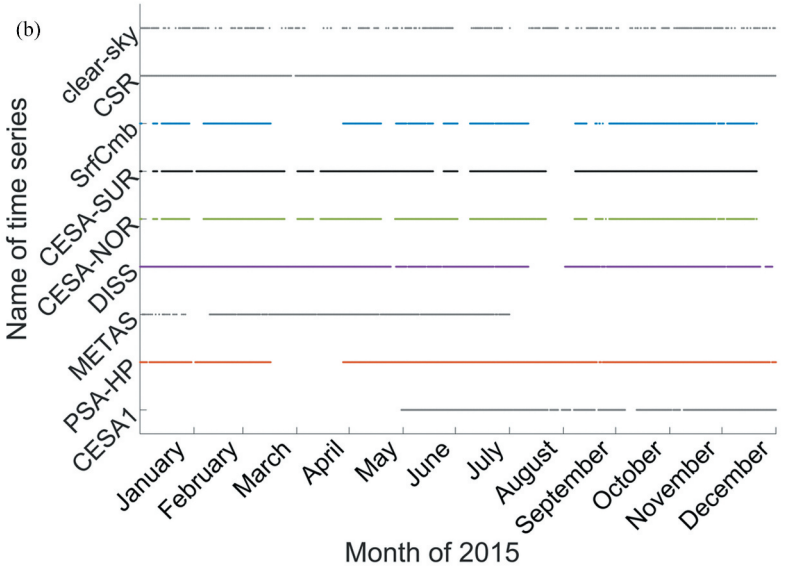
(b)
Name of time series
clear-sky
CSR
SrfCmb
CESA-SUR
CESA-NOR
DISS
METAS
PSA-HP
CESA1
January
February
March
April
May
June
July
August
September
October
November
December
Month of 2015

the more temporarily representative dataset that our conclusions are not biased by some time of year being underrepresented.

At Payerne, similar quality assessment is made, although as mentioned, only a single pyrheliometer is used and it is not possible to test spatial representativeness. Vuilleumier et al. (2014) investigated the accuracy of the Payerne solar irradiance measurements. They found that DNI expanded uncertainty is less than 1.5%, while global and diffuse horizontal irradiance (GHI and DfHI) uncertainties are less than 1.8%. They described in detail the Payerne measurements used in this study. Because of the observance of the strict BSRN guidelines, 98.5% of PAY DNI data at solar zenith angles less than 90° are valid in 2015. PAY data allow checking if findings from PSA where sun shines frequently can be confirmed at PAY where cloudiness is frequent.

The HelioMont validation is performed separately for clear-sky periods and for all-sky periods. To identify the clear-sky periods, we have adopted the approach of Long and Ackermann (2000) based on surface shortwave GHI and DfHI. At PSA, these were obtained from a combined dataset using the same approach as described above for DNI. Figure 1(b) shows the resulting clear-sky periods at PSA in 2015.

2.3. Circumsolar irradiance

Because of their field of view of about 2.5° half-opening angle, pyrheliometers measure irradiance from the direct beam plus some diffuse irradiance in the vicinity of the sun, called circumsolar irradiance (CSI). The CSR is the ratio of CSI over the measured DNI. The CSR is measured at PSA by the Sun and Aureole Measurement System (Wilbert et al. 2013). The instrument applies two geometrically and radiometrically calibrated digital cameras to take high dynamic range photos of the solar disk and the circumsolar region. One camera is directly facing the sun and used for the solar disk. The other camera takes photos of a screen on which an image of the circumsolar region is projected by an additional lens. The screen features a beam dump (a blackened cavity) in its centre where the image of the solar disk is projected. Both cameras use 670 nm bandpass filters. The photos are combined to obtain a radially averaged solar radiance profile of the solar disk and the circumsolar region at 670 nm. This radiance profile is converted to broadband radiance using the method from Wilbert et al. (2013) and integrated to obtain the CSR. Figure 1(b) shows the availability of CSR measurements at PSA in 2015.

To correct the in situ measured DNI for the CSI contribution, the CSI component was subtracted according to $I_{disk} = (1 - R_{CS})\, I_{meas}$, where I_{disk} is the direct normal irradiance for

Figure 1. (*a*) The MSG-SEVIRI pixel region comprising the PSA site and the positions of the four pyrheliometers used in this study, superimposed on a Google™ Earth image. (*b*) Overview of clear-sky periods and of the available CSR and DNI measurements at PSA for each station within PSA from January to December 2015. DNI measurements from stations CESA-SUR, CESA-NORTE, DISS and PSA-HP are used in this study. The mean DNI ('SrfCmb') is calculated when valid data from all four instruments are available, representing 43.2% of times when solar zenith angle is less than 90º. DNI measurements from stations CESA1 and METAS are disregarded, as using them would strongly reduce the number of time periods during which simultaneous measurements from all pyrheliometers are available.

the solar disk only, i.e. corrected for the diffuse irradiance component, I_{meas} the measured DNI and R_{CS} is the CSR. Our study is, to our knowledge, the first validation of satellite-derived DNI using a measurement-based circumsolar correction. At PAY, CSR data are not available and such a correction cannot be applied.

2.4. Aerosol optical properties

As mentioned above, the original version of HelioMont used a climatology of AOD at 550 nm from Kinne (2008) as input data. This climatology is now obsolete. Since the beginning of the century, AOD in Europe generally decreased by amount depending on the location but sometimes as much as 0.05 for average AOD typically about 0.2 (Filonchyk et al. 2019; Rizza et al. 2019). The Kinne climatology may thus overestimate AOD for recent years. Moreover, because it is a climatology, short-term (e.g. day-to-day) variability is poorly represented. Since aerosol optical properties, especially AOD, are influential, we required more accurate AOD datasets for our analysis.

We compared HelioMont results using the original climatology with results using a state-of-the-art globally available dataset or using time series of local AOD measurements. Mueller and Traeger-Chatterjee (2014) compared measured DNI and GHI at nine stations with estimation from an algorithm that used different AOD climatologies as input, including the Kinne climatology and AOD data from the Monitoring Atmospheric Composition and Climate (MACC) project. They found that agreement with the measured data was significantly better using the MACC AOD data than the AOD from climatology, especially for DNI. On the other hand, Mueller, Pfeifroth, and Traeger-Chatterjee (2015) found that assuming a fixed AOD of 0.18 resulted in a more accurate estimate of surface solar irradiance than using MACC AODs, but they linked this with the aerosol scattering affecting the algorithm cloud treatment and being already partially included in the effective cloud albedo.

Global AOD datasets at several wavelengths, including 550 nm, are available at 0.5° horizontal resolution from CAMS. CAMS is a service established to provide global data for helping air quality and climate change research. It is an outcome of the MACC project. It combines satellite and other observations into a data assimilation modelling system in order to provide daily analyses and forecasts. Eskes et al. (2015) describe the MACC project as well as the validation of its product. CAMS relies on a chemical and transport model coupled with the Emission Database for Global Atmospheric Research (EDGAR) and the Speciated Particulate Emission Wizard (SPEW), but the quality of the product is ensured by assimilation of satellite-retrieved aerosol optical depth from the Moderate Resolution Imaging Spectroradiometer (MODIS [Bellouin et al. 2013; Kosmopoulos et al. 2018]).

For measured AOD at PSA, we used sun photometer measurements from AERONET. AERONET is a global network of sun photometers that measure optical properties of the atmospheric aerosol (Holben et al. 1998). The AERONET station Tabernas, situated at PSA, provides the AOD at multiple wavelengths, and we used the Level 1.5 AOD time series. These time series contained several gaps of more than 24 hours caused mostly by cloudy periods impeding the AOD determination. We filled these gaps with AOD measured at the near-by Granada AERONET station (about 100 km west of PSA) or, if AOD measurements of neither Tabernas nor Granada were available, with AOD measurements from the Málaga AERONET station (about 200 km west of PSA). Most of the AOD data from

February to April 2015 originated from Málaga, as neither Tabernas/PSA nor Granada provided AOD measurements in this period. By screening AOD values larger than 1.2, we removed instances where the AERONET cloud filter algorithm misclassified clouds as aerosol.

At Payerne, AOD at multiple wavelengths is measured with precision filter radiometers (PFR, [Ruckstuhl et al. 2008]) and we applied a procedure similar to the one followed for PSA. However, determination of AOD via sun photometry can only be performed when no clouds, even thin ones, obscure the sun as mentioned above. At Payerne, this significantly reduces the times when directly measured AOD is available, and given the challenging topography in Switzerland, it was not possible to find another AOD measuring station sufficiently close from Payerne to complete the AOD dataset. Thus, directly measured AOD was only available for a limited fraction of times at Payerne, and AOD values for other times were interpolated, which may not represent actual conditions for some periods.

Using the original Kinne AOD climatology, the in situ measured AOD data and the CAMS dataset allowed evaluating the influence of this input when validating the HelioMont DNI estimates. Time series of AOD at 550 nm from the three datasets are shown in Figure 2 for PSA. (Because AERONET does not provide AOD at 550 nm, interpolation from neighbouring wavelengths were used.) It is remarkable that the climatological AOD and the CAMS AODs significantly overestimate the annual mean AOD when compared to the 2015 mean AERONET AOD, which may in part be related to inter-annual variability.

In addition, we also explored the AOD wavelength dependencies. With the default libRadtran aerosol mix, the AOD wavelength dependence corresponds to an aerosol

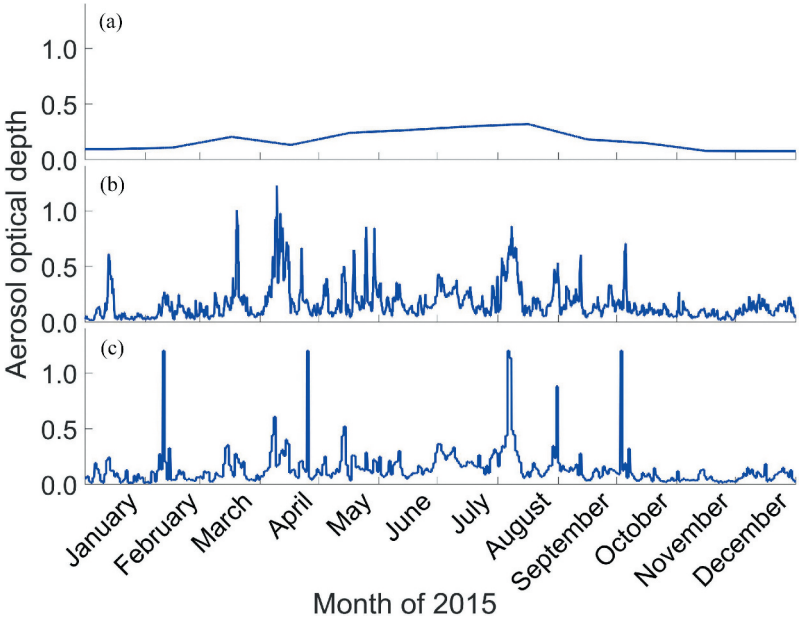

Figure 2. Aerosol optical depth at PSA in 2015: (*a*) Estimation based on Kinne climatology (annual mean is 0.180); (*b*) Estimation based on CAMS (annual mean is 0.169); (*c*) AERONET measurements (annual mean is 0.142).

Angstrom exponent parameter of $\alpha = 1.1$. However, the aerosols at PSA are sometimes strongly influenced by dust, typically Saharan dust, or can be more common aerosol of rural type or influenced by pollution. This leads to a significant variability in the wavelength dependence and the corresponding Angstrom exponent. The availability of AOD measurements at multiple wavelengths allowed us testing how influential the AOD wavelength dependence was, i.e. whether HelioMont using the default wavelength dependence assumed in libRadtran was the source of a significant uncertainty. Because HelioMont does not allow Angstrom exponent as input, we used libRadtran with setting identical to those used for constructing the HelioMont algorithm (Stöckli 2013). With the AOD measurements at multiple wavelengths, we derived a time series of α (Angstrom exponent) and β (AOD at 1 µm) at PSA and PAY in 2015. For clear-sky events, we first used the libRadtran model with a fixed α of 1.1 (default value) and the same AOD at 550 nm as used by HelioMont for checking that we reproduced HelioMont clear-sky DNI values. Then, we recomputed the DNI values for the same events, using the same libRadtran input parameters, except the Angstrom α, which was replaced by the value obtained from the multi-wavelength fit instead of being the default. Figure 3 shows the distribution of the resulting Angstrom coefficient at PSA for 2015. The peak at low α values of about 0.4 is the contribution of large aerosol particles, in particular of Saharan mineral dust aerosol. The broad peak at high α values (mode at $\alpha = 1.4$) is created by smaller aerosol particles, such as from urban pollution plumes. The highest β values correspond to low α values, which is consistent with high AOD episodes corresponding to Saharan dust events. While an α value of 1.1 could be about appropriate for PSA as an average, it does not represent well the widespread, almost bimodal, distribution of the Angstrom exponent. On the other hand, at PAY Saharan dust

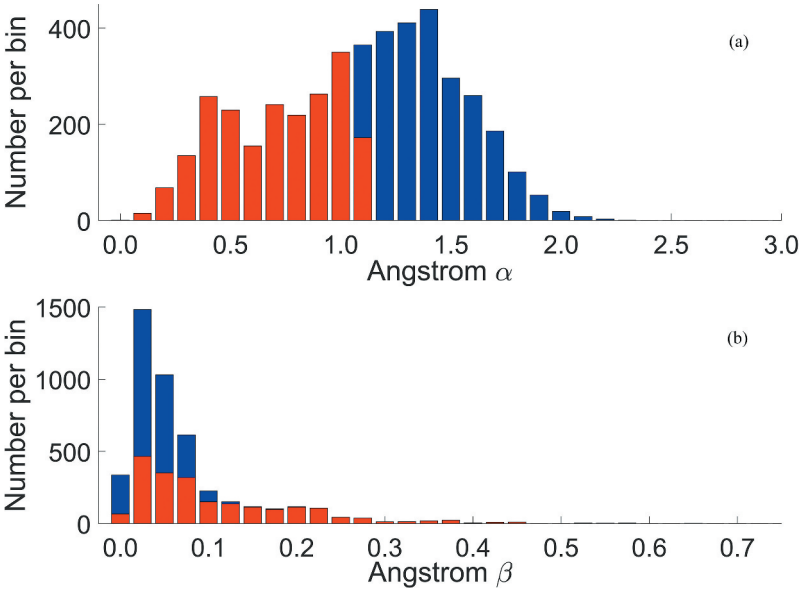

Figure 3. Aerosol Angstrom parameters distribution at PSA: (*a*) Angstrom α; (*b*) Angstrom β. Observations corresponding to α values lower (higher) than the libRadtran default of $\alpha = 1.1$ are shown in red (blue).

events are less frequent and there are few low α values with only a peak around $\alpha = 1.4$ (not shown).

3. Results and discussion

Many aspects of the HelioMont algorithm were tested because the algorithm in itself is complex, and its validation had to reflect this complexity. To help understand how the various results given and discussed in this section relate to each other, a flowchart of the algorithm is given in Figure 4 together with the main elements of the validation.

3.1. Clear-sky DNI

Figure 5 compares the PSA distributions of the four pyrheliometer average of the measured CSR-corrected clear-sky DNI to the corresponding HelioMont clear-sky DNI estimates derived using the different AOD datasets as described above in the form of probability density function and boxplots (see figure caption). It includes the libRadtran estimates with both measured AOD and measured Angstrom exponent ('meas AOD + α'). The measured DNI distributions of the four pyrheliometers are extremely similar and only the distribution of the averages is presented for simplicity (only times when valid measurements are available from the four pyrheliometers are used and every data point from this distribution is the average of the four pyrheliometer measurements).

Table 2 gives statistics of the DNI distributions for PSA, while Table 3 gives them for PAY. The clear-sky DNI derived by HelioMont using the Kinne AOD is strongly underestimated (HelioMont Kinne 25th percentile is 130 W m^{-2} lower than 25th percentile of 4 pyrheliometer average, median of HelioMont Kinne is 104 W m^{-2} lower than median of four pyrheliometer average and there is a 91 W m^{-2} difference for the 75th percentile). The CAMS-based HelioMont DNI is also underestimated, but less strongly (Comparing HelioMont CAMS with four pyrheliometer average shows differences of 31 W m^{-2}, 30 W m^{-2}, and 19 W m^{-2} for 25th percentile, median, and 75th percentile, respectively). This is in agreement with Figure 2, which shows that both of these AOD time series overestimate the AOD actually measured by the AERONET sun photometer at PSA. The average AOD at 500 nm for 2015 was 0.121 while the yearly average of the entire data set since 2011 is 0.123 (AERONET 2020). As there is hence no indication that 2015 was a year of particularly low aerosol load at PSA, the Kinne and CAMS AOD time series seem to systematically overestimate the aerosol load at PSA, leading to an underestimation of the satellite-derived clear-sky DNI. But using Kinne AOD leads to clear-sky DNI underestimation of the order of 100 W m^{-2} to 130 W m^{-2}, while for CAMS AOD the underestimation is reduced to 20 W m^{-2} to 30 W m^{-2} or about 3%.

These results are based on CSR-corrected DNI average of 4 pyrheliometers (maximizing spatial representativity), when using the pyrheliometer combination maximizing data time availability, results are nearly identical (all percentile and median differences within 5 W m^{-2} from what given above). When using non-CSR-corrected DNI, these are slightly larger leading to larger differences, but by 5 W m^{-2} to 8 W m^{-2}, which is not significant given the measurement uncertainty (Vuilleumier et al. 2014). Figure 6 shows the distribution of CSR as measured at PSA. The circumsolar irradiance accounts for 3% in median of the in situ measured DNI at PSA for all-sky conditions, but for clear-sky, the median CSR

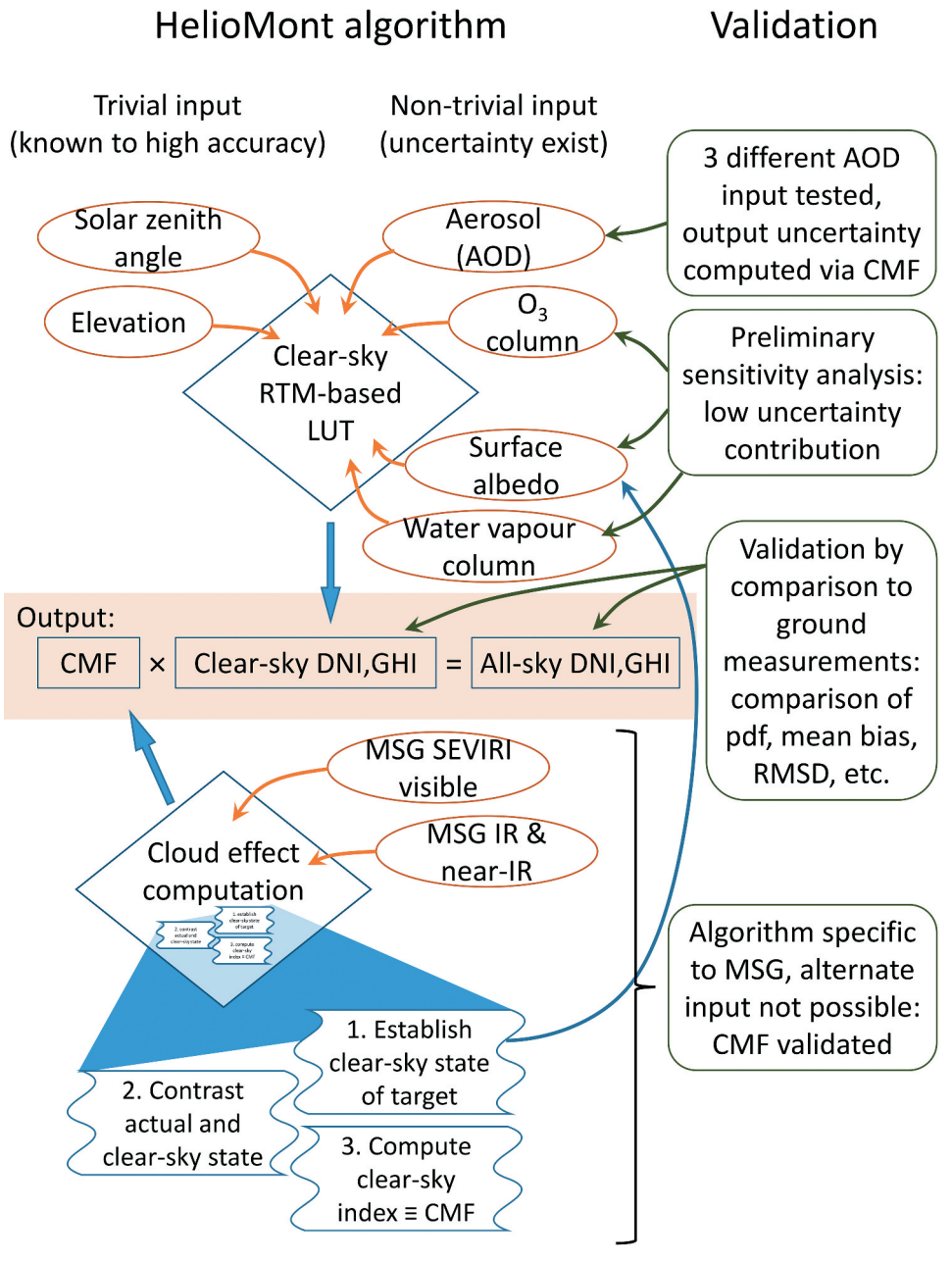

Figure 4. HelioMont algorithm flowchart with clear-sky part at top and cloud effect computation at bottom and algorithm output in the middle. Corresponding main validation steps are given on the right: AOD input test results are given in the clear-sky result section, including CMF-based subsection for uncertainty computation. The preliminary sensitivity analysis is mentioned in the clear-sky subsection, but not described in detail. Results of the validation by comparison to ground measurements are given in the clear-sky and all-sky result section and compared to results of other studies in the last subsection of the result and discussion section. The CMF resulting from the cloud effect computation is validated in the CMF-based all-sky validation result subsection. The circumsolar radiation effect is found to be negligible for clear-sky and small for all-sky (mentioned in corresponding result and discussion subsections).

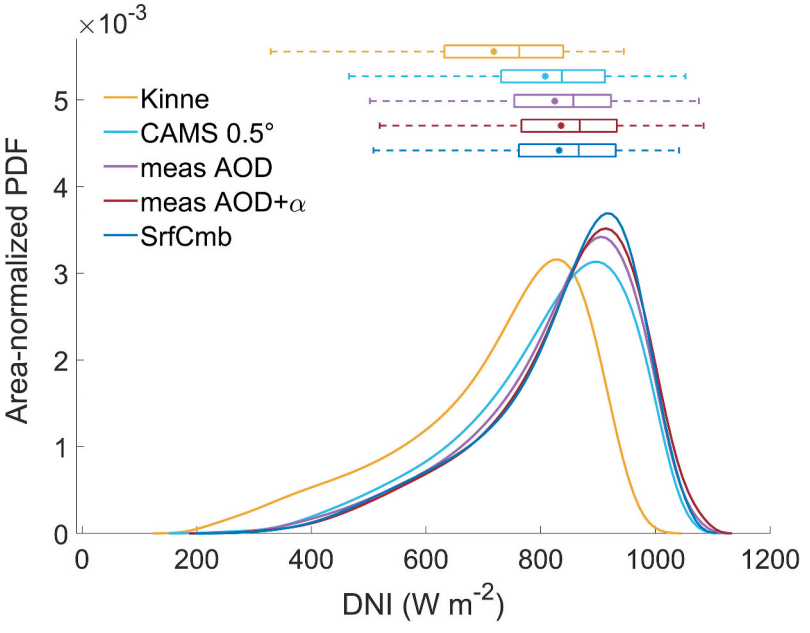

Figure 5. Kernel-density estimates of the probability density functions (PDF) of HelioMont-derived and in situ measured clear-sky DNI at PSA for the 1585 times of simultaneous availability in 2015, and corresponding box plots: The box and middle line correspond to the 25th, 50th (median) and 75th percentile while the asterisk mark represents the distribution mean. The whiskers extend to the median ±1.5 times the interquartile range or the last point of the distribution (whichever is closest to median).

Table 2. Statistics of the distributions (25th percentile, median, 75th percentile and average) for the different PSA DNI estimates and measurement datasets analysed, as well as correlation, mean absolute bias and mean bias between the HelioMont (or libRadtran) dataset and the average of the four pyrheliometers (see Table 1) at PSA.

DNI estimate or measurement	25% tile (W m^{-2})	Mean (W m^{-2})	Median (W m^{-2})	75% tile (W m^{-2})	RMSD Helio-Mont SrfCmb (W m^{-2})	Correlation HelioMont SrfCmb [f]	MAB Helio-Mont SrfCmb (W m^{-2})	Mean Bias HelioMont SrfCmb (W m^{-2})
Clear-sky								
Kinne[a]	631.8	718.1	762.5	839.4	128.1	0.9279	116.5	−114.0
CAMS[b]	730.9	807.9	836.8	911.9	59.1	0.9246	44.6	−24.2
meas AOD[c]	753.7	824.7	856.9	922.4	44.4	0.9484	30.8	−7.4
meas AOD+α[d]	766.3	835.5	868.0	932.7	39.6	0.9570	26.6	3.4
SrfCmb[e]	761.8	832.1	866.4	930.8				
PSA-HP	756.5	828.2	863.3	926.7				
DISS	762.2	832.0	866.7	930.8				
CESA-NORTE	770.7	838.4	872.0	937.4				
CESA-SUR	759.3	829.9	864.1	928.1				
All-sky								
Kinne[a]	218.5	517.4	627.2	782.5	194.4	0.8449	134.3	8.3
CAMS[b]	230.1	553.3	667.4	841.3	183.0	0.8738	110.4	44.2
meas AOD[c]	238.0	564.1	687.5	850.7	186.3	0.8737	104.1	55.0
SrfCmb[e]	70.8	509.1	614.8	841.8				
PSA-HP	59.9	506.3	612.1	840.9				
DISS	61.5	508.6	618.8	844.7				
CESA-NORTE	59.2	512.5	625.0	847.6				
CESA-SUR	59.2	509.2	622.6	842.8				

Table 3. Statistics of the distributions (25th percentile, median, 75th percentile and average) for the different PAY DNI estimates and measurement datasets analysed, as well as correlation, mean absolute bias and mean bias between the HelioMont (or libRadtran) dataset and the ground-based measured DNI.

DNI estimate or measurement	25% tile (W m^{-2})	Mean (W m^{-2})	Median (W m^{-2})	75% tile (W m^{-2})	RMSD Helio-Mont PAY SWdir (W m^{-2})	Correlation HelioMont PAY SWdir [e)]	MAB Helio-Mont PAY SWdir (W m^{-2})	Mean Bias HelioMont PAY SWdir (W m^{-2})
Clear-sky								
Kinne[a]	548.4	650.0	693.7	778.4	154.5	0.9586	145.9	−145.8
CAMS[b]	700.3	780.9	817.8	894.4	65.6	0.9114	49.6	−14.9
meas AOD[c]	698.5	782.3	820.0	896.6	33.9	0.9785	25.3	−13.5
meas AOD $+\alpha$ [d]	707.5	788.9	823.6	899.8	30.9	0.9779	23.7	−6.9
PAY SWdir	705.5	795.8	837.6	910.6				
All-sky								
Kinne[a]	0.0	312.8	203.7	635.8	177.4	0.8676	109.4	−5.5
CAMS[b]	0.0	359.4	252.1	720.5	183.8	0.8728	103.0	41.1
meas AOD[c]	0.1	365.4	265.0	731.2	186.2	0.8718	99.9	47.1
PAY SWdir	0.0	318.3	99.0	690.3				

[a]HelioMont DNI estimate using AOD from Kinne climatology
[b]HelioMont DNI estimate using AOD from CAMS
[c]HelioMont DNI estimate using measured AOD
[d]libRadtran DNI estimate using measured AOD and measured AOD Angstrom exponent
[e]Pearson's correlation coefficient *r*

correction is only 0.5%. The clear-sky CSR correction becomes larger for the events with the largest AOD, but it remains of the order of 2% only. The results at PAY are relatively consistent with those obtained at PSA with slightly larger differences between HelioMont Kinne and pyrheliometer measurements (differences of 157 W m^{-2}, 144 W m^{-2}, and

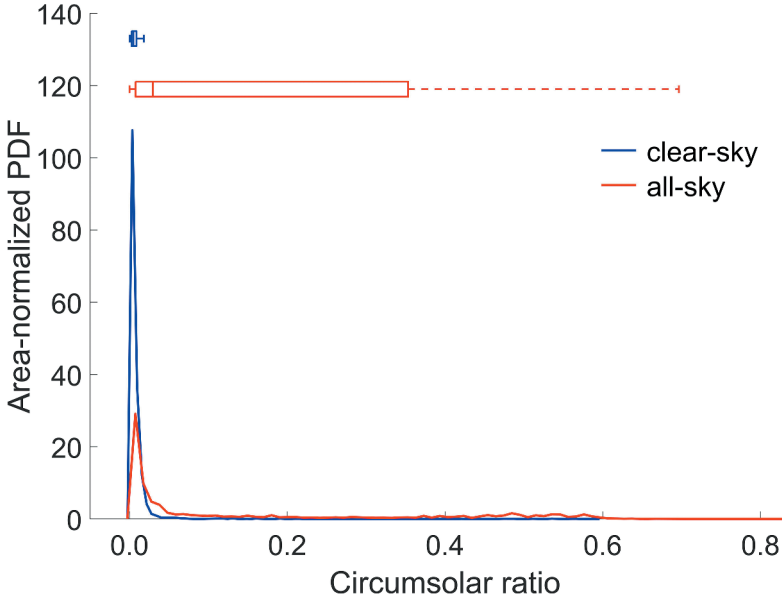

Figure 6. Kernel-density estimates of the CSR PDF. PDF and boxplots produced in the same way than for Figure 5.

132 W m^{-2} for 25th percentile, median, and 75th percentile, respectively) and similar for HelioMont CAMS (5 W m^{-2}, 20 W m^{-2}, and 16 W m^{-2} for 25th percentile, median, and 75th percentile, respectively).

When using the measured AOD to estimate DNI at PSA, very good agreement with ground-based measured DNI is obtained. The HelioMont DNI estimation using measured AOD values ('meas AOD' on Figure 5) is slightly below measured DNI (differences of 8 W m^{-2}, 10 W m^{-2}, and 8 W m^{-2} for 25th percentile, median, and 75th percentile, respectively), while using libRadtran with both measured AOD and measured Angstrom exponent ('meas AOD + α' on Figure 5) yields even better agreement (differences of −4 W m^{-2}, −2 W m^{-2}, and −2 W m^{-2} for 25th percentile, median, and 75th percentile, respectively). However, all these differences are within measurement uncertainty, and it is thus not possible to assert that the improvement related to using measured Angstrom exponent is significant. Using other statistical measures (correlation, mean absolute bias, RMSD) as well as other DNI measurement dataset (combination maximizing data time availability) also show an excellent agreement within measurement uncertainty. When using non-CSR corrected DNI as reference, the differences for HelioMont DNI estimation with measured AOD values are at the limit of the DNI measurement uncertainty (16 W m^{-2}, 15 W m^{-2}, and 13 W m^{-2} for 25th percentile, median, and 75th percentile, respectively), while for libRadtran with both measured AOD and measured Angstrom exponent the differences are well within measurement uncertainty. At PAY, very good agreement is also obtained, and it is impossible to make a difference between HelioMont DNI estimation using measured AOD and libRadtran estimation with both measured AOD and measured Angstrom exponent (all differences of the order of 10 W m^{-2} to 18 W m^{-2}).

We have also tested the radiative transfer scheme sensitivity with respect to changes in total column water vapour and total column ozone by varying both variables independently within reasonable limits. The resulting effects on the clear-sky DNI distribution and mean absolute bias were negligibly small.

The results above demonstrate agreement for clear-sky DNI value that ranges from 'acceptable' (HelioMont Kinne) to 'good' (HelioMont measured AOD). However, it would be useful to develop a quantitative measure of this agreement that would be similar to the uncertainty for measurements. This can be achieved by assessing the difference between the measured value and the theoretical clear-sky estimate. We found that a tool for validating all-sky values and particularly the effect of clouds can also provide a measure of agreement for clear-sky cases. As mentioned earlier, HelioMont first makes a theoretical clear-sky estimate and then multiplies it by a factor reflecting the effect of clouds, which we call here CMF (it corresponds to HelioMont clear-sky index). In order to validate HelioMont satellite-derived DNI CMF (in all-sky situations), we computed a ground-based derived CMF by dividing the surface measured DNI by HelioMont theoretical clear-sky estimate. Figure 7 illustrates this by an example taken on 24 February 2015. On this day most of the morning was classified as clear-sky by the Long and Ackermann (2000) algorithm, while from about midday a thin cloud cover builds up. The ground-based measured DNI (average of four pyrheliometers) is shown with dots that are red if this measurement is clear-sky and blue for other measurements. The HelioMont clear-sky theoretical estimates have been interpolated for all ground-based measurement times and are shown as the black line. For the period between 09:30 and

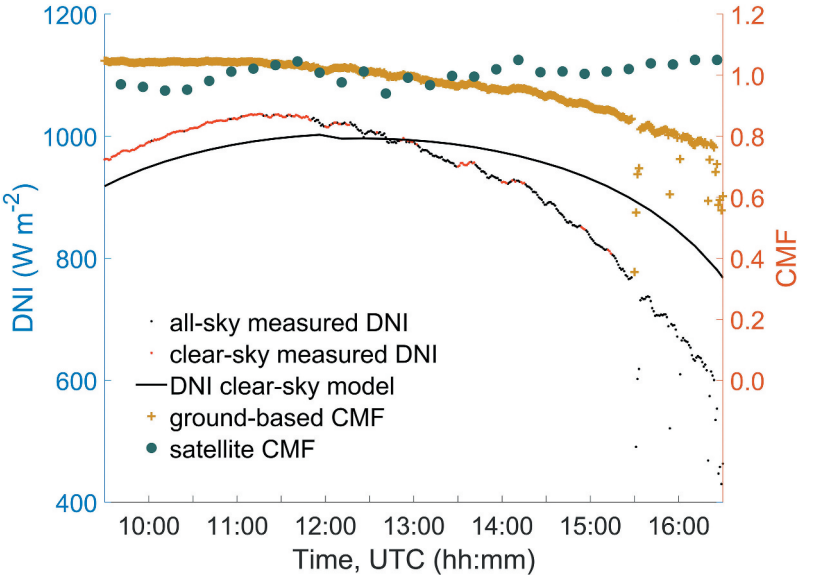

Figure 7. DNI (left-hand scale) and corresponding CMF (right-hand scale) at PSA on 24 February 2015 including DNI ground-based measurements (red and blue dots), theoretical DNI clear-sky estimates (black curve), CMF derived by dividing measurements by theoretical clear-sky estimates (yellow crosses) and CMF derived from satellite imagery (dark green bullets). Coordinated Universal Time (UTC) is used for the *x*-axis.

11:30 (UTC), when only clear-sky times are detected, the HelioMont clear-sky estimate is underestimated by about 50 W m^{-2} (about 5%). It should be noted that, as a coincidence, local AOD measurements were not available and AERONET data from the station of Málaga were used instead, which may explain the clear-sky underestimation. After 11:30, the cloud cover builds up (thin clouds) and the measured DNI becomes significantly lower than the clear-sky estimate. The validation CMF (measured DNI divided by clear-sky estimate) is shown with the yellow crosses. It is a little higher than 1 in the morning and goes down to values of the order of 0.6 to 0.8 after 15:30. The fact that the CMF is slightly above 1 in the morning indicates the slight underestimation of the clear-sky DNI. The satellite-based (HelioMont) CMF is shown as the dark green bullets. In this case, the cloud cover seems not to have been detected by HelioMont (a weakness that is discussed in our analysis of all-sky cases) and the corresponding CMF value stays around 1 for the entire period shown on the figure. The CMF validation is based on comparing such satellite and ground-based CMF.

3.2. CMF-based clear-sky validation

If clear-sky cases are tested (satellite and ground-based CMF should ideally be equal to one), it is actually more interesting to test the inverse of the CMF. First, if the clear-sky CMF distribution is relatively well centred on one and symmetrical, it makes little difference to test the CMF or its inverse value, and the ground-based derived inverted CMF directly provides information on the uncertainty of the theoretical HelioMont (or

libRadtran) clear-sky estimate. Under assumptions that the uncertainty contributions to the variance can be linearized and that the uncertainty is statistically well behaved,

$$\frac{1}{K_{cs}^{val}} = f\left(I_{cs}^{th}, I_{cs}^{meas}\right) = \frac{I_{cs}^{th}}{I_{cs}^{meas}} \Rightarrow$$
$$\sigma^2(f) = \left(\frac{\partial f}{\partial I_{cs}^{th}}\right)^2 \sigma^2\left(I_{cs}^{th}\right) + \left(\frac{\partial f}{\partial I_{cs}^{meas}}\right)^2 \sigma^2\left(I_{cs}^{meas}\right) = \frac{\sigma^2\left(I_{cs}^{th}\right)}{\left(I_{cs}^{meas}\right)^2} + \left(\frac{I_{cs}^{th}}{I_{cs}^{meas}}\right)^2 \frac{\sigma^2\left(I_{cs}^{meas}\right)}{\left(I_{cs}^{meas}\right)^2} \quad (1)$$

where K_{cs}^{val} is the clear-sky validation ground-based derived CMF expressed as a function f of the DNI theoretical clear-sky estimate I_{cs}^{th} and of the DNI ground-based measured value I_{cs}^{meas}. The first part of the right-hand term in the second line of Equation (1) is the variance due to the uncertainty of the theoretical clear-sky estimate divided by the measured clear-sky irradiance. Because for clear-sky events the measured irradiance is close to the theoretical estimate, this term is approximately the relative variance due to the uncertainty of the theoretical clear-sky estimate and its square root gives an estimate of the relative standard uncertainty. The second part is the inverted squared CMF multiplied by the relative variance due to the uncertainty of the measurement. The inverted squared CMF is about one because the CMF itself is about one for clear-sky case; thus, the second part of the right-hand term is approximately equal to the square of the relative measurement uncertainty. Then, the distribution of the inverted ground-based derived CMF gives the combined effect of the relative uncertainties of the theoretical clear-sky estimate and the ground-based measurements. For DNI – it should be noted that the same approach is applicable to GHI – Vuilleumier et al. (2014) showed that the relative measurement expanded uncertainty for large signals (e.g. clear-sky cases) is on the order of or less than 1.5%. Including the uncertainty introduced by approximating the CMF to one, one can conservatively assume that the contribution of the second part of the right-hand term is limited to the square of 2% to 3%.

Figure 8 shows a comparison between the satellite and ground-based derived 15-minute averaged inverted CMF for clear-sky cases. On Figure 8(a), the measured AOD is used as input for the theoretical clear-sky estimate, and on Figure 8(b), the CAMS AOD is used as input. We repeated this analysis using different options and Figure 8 shows only one of our results, but it is typical of what we obtained. Specifically, we tried all three time aggregations mentioned in the data and methods section

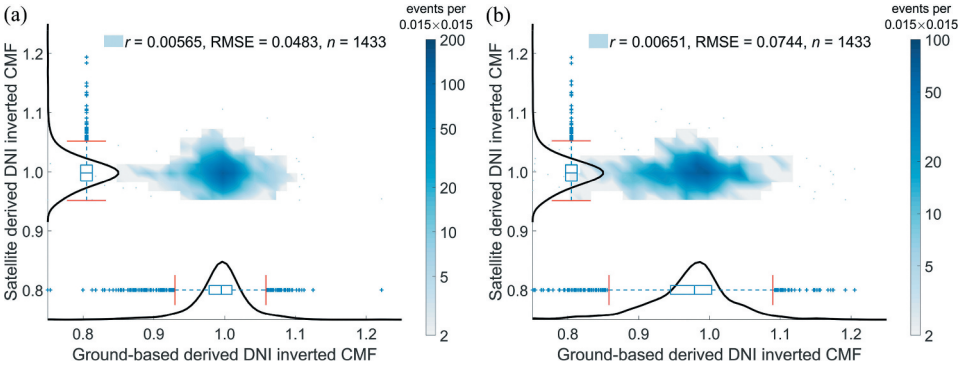

Figure 8. DNI inverted CMF at PSA using HelioMont with measured AOD (*a*) and CAMS AOD (*b*): satellite-derived vs. ground-based derived and corresponding estimated PDF and box plots.

(1-minute, 15-minutes and 1-hour average comparisons). The three time averaging strategies yielded similar results, except that the outliers – distribution tails – changed. Similarly, we used two different solar elevation cuts: the correspondence between satellite and ground-based derived CMF is sensitive to the solar elevation angle. At small elevation angles, clouds far from the satellite pixel corresponding to the ground-based measurement location can influence the measured value, significantly increasing the uncertainty. Times considered for the CMF comparisons were restricted based on the solar elevation angle and two cut-off values were considered: 10° and 15°; the latter cut being applied here. Figure 8 shows the two-dimensional distribution of inverted satellite-derived CMF versus inverted ground-based derived CMF. It is divided into 0.015 × 0.015 intervals for which the density is colour-coded in log-scale. For intervals where the number of points is less than two, the points are individually shown. In addition, the inverted CMF distributions and corresponding boxplots are given along the *x*- and *y*-axis for ground-based and satellite-derived CMF, respectively, allowing the estimation of uncertainty. More events are included in the tails of the distributions than would be the case for normal distributions with the same standard deviation. Different methods for estimating the expanded uncertainty were tested including the standard deviation multiplied by $k = 2$, the 2.5% to 97.5% range, and the range based on the boxplots. The latter (essentially using the median ± the interquartile range multiplied by 1.5) proved to be the most robust estimate of the expanded uncertainty with very little variation when changing the time aggregation strategy and only a modest increase when changing the solar elevation cut from 15° to 10°.

These estimates are shown with red lines in Figure 8 and include 91% and 97% of the distribution for ground-based and satellite CMF, respectively. When using measured AOD as input for the theoretical clear-sky estimates, the inverted CMF is very well centred on 1 (medians are 0.995 and 0.998 for satellite and ground-based CMF, but using different combinations of instruments and selection of events made the median for ground-based inverted CMF change by up to 2%). The box plot ranges are ±6.5% and ±5% for ground-based and satellite-derived inverted CMF, respectively (±7% and ±5% when using a solar elevation cut value of 10°). The good results obtained for satellite-derived CMF show that the clear-sky situations that were identified using the ground-based GHI and DfHI measurements are well recognized by the HelioMont algorithm. From ground-based derived CMF, we can deduce that the expanded uncertainty of the clear-sky DNI estimate is about 6% when using measured AOD as input, considering the small contribution from the measurement uncertainty to the CMF uncertainty. When using CAMS AOD as input for theoretical clear-sky estimates, only the ground-based derived inverted CMF changes (the same events are used in both cases). The median is displaced by about 2% to 0.979 and the box plot range is about ±12% around the median (including 95% of events). In this case, the contribution from the measurement uncertainty is negligible, and this should be considered as the expanded uncertainty of the theoretical DNI estimate when using CAMS AOD as input.

The same analysis conducted for Payerne yielded similar results. For satellite-derived inverted CMF, the median is 0.996 with a range of about ±5.5% around it, including 96% of the events. For ground-based derived inverted CMF, the median is 0.983 with a range

around it of ±5% including 94% of the distribution when using measured AOD as input, while the median is 0.986 with a range around it of ±15% including 97% of the distribution when using CAMS AOD as input.

3.3. All-sky DNI

Similarly to Figures 5, Figure 9 compare the distributions and the corresponding boxplots of the in situ measured CSR-corrected all-sky DNI to the HelioMont all-sky DNI derived for the PSA site using different AOD datasets. Only events when all the datasets are simultaneously available are used, and similarly to Figure 5, only the distribution of the averages of the four pyrheliometer measurements is presented (SrfCmb). PSA all-sky distributions are bi-modal with one relatively wide peak at high values corresponding mainly to events when the sun is not masked by clouds, and a sharp peak near zero corresponding to events when the sun is masked. At PAY (not shown), the distributions are similar, except that the high-value peak is weak with values around 800 W m^{-2} to 900 W m^{-2} only twice higher than values in the region 200 W m^{-2} to 400 W m^{-2}. The HelioMont-derived DNIs differ from the pyrheliometer-measured distribution in two ways: first, what was already observed for clear-sky data is reproduced in the high-DNI peak; the second main difference involves the sharp peak at zero or near-zero DNI. For HelioMont-derived DNI, this peak is about half as high as for measured DNI. HelioMont significantly underestimates the frequency of almost-zero DNI periods. This affects the boxplots in producing significantly higher 25th percentile and median for the HelioMont-derived DNI than for the measured DNI (HelioMont Kinne

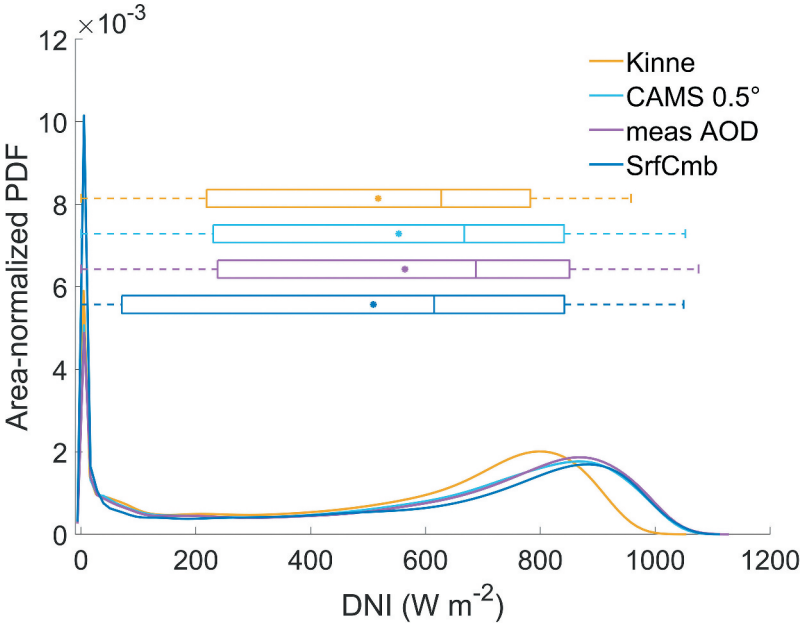

Figure 9. Kernel-density estimates of the PDF and corresponding boxplots of HelioMont-derived and in situ measured all-sky DNI at PSA for the 7603 simultaneously available events in 2015. PDF and boxplots produced in the same way than for Figure 5.

25th percentile and median are 148 and 12 W m^{-2} higher than 25th percentile of four pyrheliometer average, while HelioMont CAMS 25th percentile and median are 159 and 52 W m^{-2} higher, and HelioMont measured AOD 25th percentile and median are 167 and 73 W m^{-2} higher). Although the boxplots show there is a disagreement on the low irradiance end of the DNI distributions, it does not show that this disagreement is mainly due to differences in the number of near-zero DNI. Furthermore, studying the mean bias provides a misleading conclusion: The smallest mean bias with respect to measurements is for HelioMont Kinne with a mean bias of only 8.3 W m^{-2} (Table 2). However, this is due to compensating errors between underestimation of the number of near-zero DNI and the peak at high DNI being displaced towards lower irradiance compared to the pyrheliometer measurements.

As was the case for clear-sky events, using the pyrheliometer combination maximizing time availability yields nearly identical results for distributions. On the other hand, using or not the CSR correction has a larger influence than for clear-sky events: the DNI pyrheliometer measurement distribution is displaced towards higher values; thus, the differences between HelioMont and measured DNI distributions in 25th percentile and median are reduced. But this reduction is again related to compensating errors because the CSR correction is influential on event with non-zero DNI, while the main source of the differences is linked to an underestimation of near-zero DNI. Results at PAY confirm that the number of near-zero DNI events is underestimated by HelioMont, but less strongly – only by about 30%. This may be because strongly overcast situations are more frequent in Payerne and HelioMont can easily identify such events.

Traditional validation methods often use statistical indicators measuring the general agreement between datasets such as mean bias, mean absolute bias, RMSD, etc. We do not favour such indicators in this case because it is difficult to identify problems such as the compensating errors mentioned above and we think the CMF-based technique described in the next section is more powerful for this. Nonetheless, in order to compare our results to those of other studies, we also provide these indicators in Tables 2 and 3 for PSA and PAY, respectively. While for clear-sky events, these indicators show that using the Kinne (2008) climatology for AOD gives the worst results and using measured AOD gives the best results at both stations, for all-sky results it is not the case. At PSA the mean bias and RMSD are 8.3 W m^{-2} and 194.4 W m^{-2} for Kinne, while they are 55.0 W m^{-2} and 186.3 W m^{-2} using measured AOD. At PAY, the mean bias and RMSD are −5.5 W m^{-2} and 177.4 W m^{-2} for Kinne, while they are 47.1 W m^{-2} and 186.2 W m^{-2} using measured AOD. This would lead to the misleading conclusion that it is better to use the Kinne (2008) climatology than measured AOD values, especially for Payerne. These results are obtained by comparing the HelioMont values with the ground-based measurements at the time closest to the SEVIRI scan time (instantaneous comparison). For RMSD, making comparison with 15-minute averages of ground-based measurements or comparing the average of four satellite values with 1-hour averages of ground-based measurements may lead to better results. We also performed such computations. The RMSD decreased from a range of 186 W m^{-2} to 194 W m^{-2} to a range of 162 W m^{-2} to 176 W m^{-2} (15 minutes) and to a range of 132 W m^{-2} to 146 W m^{-2} (1 hour) for PSA and from a range of 177 W m^{-2} to 186 W m^{-2} to a range of 164 W m^{-2} to 173 W m^{-2} (15 minutes) and to a range of 126 W m^{-2} to 132 W m^{-2} (1 hour) for PAY. While the RMSD decreased, the time averaging did not change the rankings and would not change the conclusions about the best AOD to be used.

3.4. CMF-based all-sky validation

The CMF validation technique described previously can provide more insight into the correctness of the cloud effect treatment in HelioMont. For all-sky cases, the following ground-based derived CMF is used:

$$K_{as}^{val} = \frac{I_{as}^{meas}}{I_{cs}^{th}} \tag{2}$$

In the above definition of the all-sky validation CMF (K_{as}^{val}), the *all-sky* DNI measurement (I_{as}^{meas}) is compared to the DNI theoretical *clear-sky* estimate (I_{cs}^{th}); thus, we do not expect it to be centred around 1 as in the clear-sky CMF validation subsection, but to cover the full range of CMF values. K_{as}^{val} can be used to validate K_{as}^{HM}, the value computed by HelioMont. However, for this validation to be meaningful, I_{cs}^{th} should be as accurate as possible. Previously we showed that the expanded uncertainty of I_{cs}^{th} is about 6% when using HelioMont with measured AOD as input. This clear-sky estimate is then used for the validation, but AOD is not measured when clouds are masking the sun, and the AOD had to be interpolated at those times. At PSA, interpolations were only needed for short time periods (Figure 2 shows that there are no long periods when measured AOD is not available), but at PAY longer interpolations were necessary, especially in winter, which may increase the uncertainty due to I_{cs}^{th}.

Figure 10 shows the comparisons between the HelioMont (satellite-derived) and the validation (ground-based derived) CMF for PSA (*a, b*) and PAY (*c, d*). This figure is produced in the same way as Figure 8, except that all-sky CMF is shown instead of inverted clear-sky CMF. For PSA, the CSR-corrected measurements are used for consistency with the previous subsection, but the dataset with the pyrheliometer combination maximizing data time availability is used to increase the number of available events, which is low in the intermediary region ($0.2 \lesssim \text{CMF} \lesssim 0.8$). Figure 10 (*a*) and (*c*) show the comparisons for 15-minute averages; while Figure 10(*b, d*) show 1-hour averages (refer to the explanation of Figure 8 in the previous subsection).

In all plots of Figure 10, there is a band of higher density in the lower-left corner (low CMF, and thus low DNI) that extends more along the *y*-axis (HelioMont CMF) than the *x*-axis (validation CMF). In such cases, the CMF estimated by HelioMont is higher than the CMF derived from ground-based measurements that corresponds to near-zero measured DNI, and this produces the underestimation of low-DNI events in the HelioMont distribution described above for Figure 9. Another feature visible on all plots is that the high-density region around $K_{as}^{val} = 1, K_{as}^{HM} = 1$ (cases when the sun is not masked by clouds, K_{as}^{HM} is the all-sky HelioMont-derived CMF) stretches along the *x*-axis. In such cases, the HelioMont CMF is around 1, meaning no clouds have been detected by satellite, but the measured DNI is lower than the clear-sky theoretical estimate. The most likely explanation for this is that some thin clouds were present, but undetected by MSG/SEVIRI. A search for such events resulted in the selection of the period used in Figure 7. In a recent publication still in open review, Zou et al. (2020) compared new data from the Michelson Interferometer for Passive Atmospheric Sounding (MIPAS) to the Cloud-Aerosol Lidar and Infrared Pathfinder Satellite Observations (CALIPSO), already an instrument sensitive to thin cirrus cloud. They claim that 'MIPAS observed twice as many stratospheric cirrus

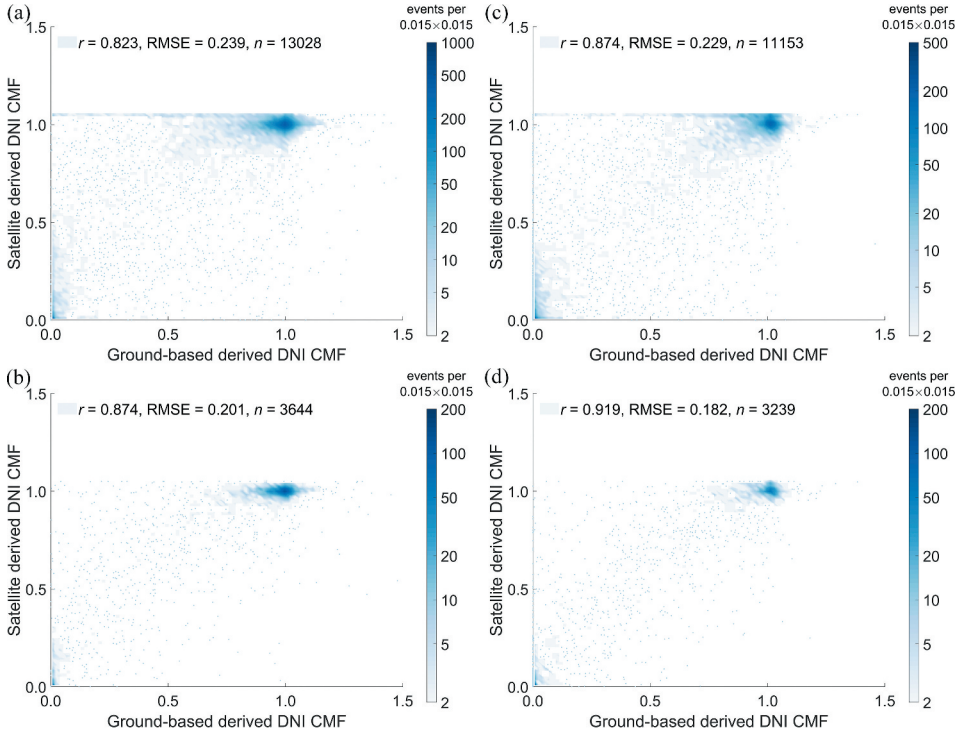

Figure 10. DNI CMF: satellite-derived vs. ground-based derived at PSA (*a, b*) and PAY (*c, d*) for 15-minute averages (*a, c*) and 1-hour averages (*b, d*). Only CMF for events at solar zenith angle less than 75° are shown.

clouds at northern and southern middle latitudes (occurrence frequencies of 4% to 5% for MIPAS rather than about 2% for CALIPSO).' Finally, the intermediary region ($0.2 \lesssim \text{CMF} \lesssim 0.8$) is sparsely populated and the spread is important, especially when using 15-minute average. When using 1-hour averages, the spread is slightly reduced as shown by the increased correlation and decreased RMSD.

Time and spatial (multiple pyrheliometers at PSA) averaging is mostly influential on the dispersion of the data in DNI and CMF comparisons. In summary, we find that both time and spatial averaging reduce the dispersion, but spatial averaging only has influence when not using time averaging; the following paragraphs describe it in more detail. For this, we analyse mainly the correlation (*r*) and RMSD (indicators sensitive to the dispersion). We also compute the standard deviation of the residual to a linear regression of HelioMont-derived vs. ground-based measured DNI. It is similar to RMSD for DNI, but only focusing on the dispersion. Table 4 gives the correlation and RMSD of CMF and DNI comparison, as well as the DNI residual standard deviation. These are given for the PSA dataset maximizing data time availability (only one pyrheliometer used), for the dataset maximizing spatial representativity (average of four pyrheliometers), and for the PAY dataset (only one pyrheliometer, but more frequent cloud situations).

As expected, the correlation increases and the RMSD decreases (as well as the DNI residual standard deviation) in all cases when increasing the averaging time,

Table 4. Dispersion-sensitive statistical indicators for HelioMont-derived vs. ground-based measured comparisons for DNI and CMF. Indicators are given for instantaneous comparisons (the 1 minute measurement closest to satellite scan-time is used), for 15-minute averages of ground measurements around scan-time and 60-minute averages of ground measurements compared to averages of HelioMont estimations for the four scan time in the hour. At PSA, both datasets maximizing data time availability (single pyrheliometer) and spatial representativity (average of four pyrheliometers) are used.

		Instantaneous	15-minute average	60-minute average
CMF correlation[a]	PSA single	0.79	0.82	0.87
	PSA multi	0.80	0.83	0.88
	PAY	0.85	0.87	0.92
CMF RMSD	PSA single	0.27	0.24	0.20
	PSA multi	0.26	0.24	0.20
	PAY	0.26	0.23	0.18
DNI correlation[a]	PSA single	0.85	0.89	0.94
	PSA multi	0.87	0.90	0.94
	PAY	0.87	0.89	0.93
DNI residual standard deviation (W m^{-2})	PSA single	173.2	150.8	111.8
	PSA multi	165.3	149.7	116.4
	PAY	173.9	163.4	120.9
DNI RMSD (W m^{-2})	PSA single	195.7	161.2	122.4
	PSA multi	186.3	161.7	131.7
	PAY	186.2	173.8	132.3

[a]Pearson's correlation coefficient *r*

[a]HelioMont DNI estimate using AOD from Kinne climatology
[b]HelioMont DNI estimate using AOD from CAMS
[c]HelioMont DNI estimate using measured AOD
[d]libRadtran DNI estimate using measured AOD and measured AOD Angstrom exponent
[e]Average of measurements from four pyrheliometer
[f]Pearson's correlation coefficient *r*
Table 2

demonstrating the diminution of the dispersion. For spatial averaging, when comparing single vs. multiple instrument at PSA, the effect is almost negligible on the CMF, but some systematic effect is present for DNI comparison in instantaneous comparisons. For the 15-minute and 60-minute averages, the effect of spatial averaging is either negligible or even reversed in some cases (the RMSD and residual standard deviations for 60-minute averages are larger when using the average of four pyrheliometers than when using a single pyrheliometer).

At PAY, for CMF, the dispersion is generally lower than at PSA (higher correlation and lower RMSD). For DNI, the dispersion is similar than for the PSA single-pyrheliometer dataset and slightly higher than for the four-pyrheliometer dataset. The different cloud regimes at PAY and PSA are the most likely cause for this. For CMF, at PSA there are many cases when the situation is clear-sky or with thin cloud coverage, which produces an accumulation of points in the region $0.5 < K_{as}^{val} < 1.2, 0.8 < K_{as}^{HM} < 1.05$ on Figure 10(a). Most of the other data correspond to situations when the sun is completely masked by clouds producing an accumulation at $K_{as}^{val} < 0.1, K_{as}^{HM} < 0.5$. At PAY, these regions also have a high concentration of points (Figure 10(c)), but they tend to stretch more along the diagonal rather than parallel to the axes as for PSA. This difference results in a lower dispersion of the CMF at PAY than at PSA and may be due to the higher diversity of cloud situations at Payerne. For DNI, when the data is not normalized using I_{cs}^{th}, the fact that

there are more clear-sky situations at PSA, which are easier to estimate with HelioMont, compensates the limitations in the identification of thin clouds (band in the CMF region $0.5 < K_{as}^{val} < 1.2, 0.8 < K_{as}^{HM} < 1.05$) compared to PAY.

Time integration longer than 1 hour (3- or 5-hour averages) does not produce further reduction of dispersion and in some cases the opposite, except if one includes night-time data in the averages. However, in the latter case, the improvement is the result of including many zero values (both for satellite-derived and ground-measured data). Together with the above analysis of spatial averaging, this suggests 1-hour time averaging has an effect similar to spatial averaging in our study. The movement of cloud shadows is a primary explanation for this. The relatively limited effect of spatial averaging is also due to spatial variability being only one in many factors leading to the dispersion between HelioMont estimates and ground-based measurements. Thus, averaging time of the order of 1 hour may be optimal when comparing data measured at one location on the ground with satellite estimates for areas of the size of a SEVIRI pixel.

The technique using a validation CMF can be applied to GHI in the same way we applied it to DNI in the analysis presented above. We briefly mention the main results for GHI without going into details. We obtain even smaller uncertainty for the clear-sky HelioMont estimate using measured AOD (of the order of ±4% compared to ±6% for DNI). This is in agreement with our finding that AOD is the main source of uncertainty for HelioMont clear-sky estimates. For DNI, aerosols only reduce the irradiance through extinction, while for GHI, part of the irradiance lost in the direct beam due to scattering is recovered as scattered diffuse irradiance. Hence, the influence of AOD uncertainty on GHI is less than on DNI. Concerning the validation of CMF for GHI, the feature in the high-density region around $K_{as}^{val} = 1, K_{as}^{HM} = 1$ (stretching along the *x*-axis) is also visible, although less clearly. On the other hand, there is no band along the *y*-axis at low CMF. On the opposite, it rather seems that HelioMont underestimates the CMF in the region of CMF less than 0.5 for GHI. We also found an improvement of the correlation and RMSD when increasing the averaging time to 1 hour, and in general, the CMF correlation and RMSD are better (higher correlation and lower RMSD) for GHI than DNI.

3.5. Comparisons with other studies

Comparing our results to those of other similar validation studies allows verifying whether our evaluation of the agreement between HelioMont DNI estimates and corresponding ground-based measurements is similar to agreement determined for other algorithms. Amillo, Huld and Müller (2014) validated DNI and GHI estimated using satellite images from the Meteosat First Generation with 10-minute averages of ground measurements from 13 BSRN stations and 3 non-BSRN stations. For DNI, they found mean bias between −25 W m^{-2} and 31 W m^{-2}, while RMSD was between 120 W m^{-2} and 151 W m^{-2}. In particular, they also used data from the Payerne station where they found a bias of 3 W m^{-2} and an RMSD of 147 W m^{-2}. This is smaller than the RMSD we found for 15-minute averages (164 W m^{-2} to 173 W m^{-2}, depending on the AOD source), which would be surprising since they used MFG data and we used MSG; but they included night data in their comparison, while we did not. Since estimates and ground measurements should all be zero for ground data, this of course strongly reduces the RMSD.

Eissa et al. (2015) compared DNI and GHI estimates from the HelioClim-3 database based on MSG data to hourly averages of ground measurements from 7 (GHI) or 2 (DNI) stations from the Egyptian Meteorological Authority (EMA). For DNI, they found mean bias between −45 W m^{-2} and 113 W m^{-2}, while RMSD was between 160 W m^{-2} and 213 W m^{-2}. These results should probably be compared to the PSA results (station within an arid environment with relatively frequent episode of Saharan dust). For PSA we found smaller mean bias (between 8 W m^{-2} and 55 W m^{-2}) and RMSD for hourly averages (between 132 W m^{-2} and 146 W m^{-2}).

Greuell, Meirink, and Wang (2013) compared DNI estimates from the SICCS algorithm derived from MSG data with ground measurements from 8 European BSRN stations. They performed a clear-sky analysis relatively similar to ours, using for AOD input either AERONET measured data or MACC data. For clear-sky measurement using AERONET data, they found a mean bias between −11 W m^{-2} and 6 W m^{-2} (Payerne not included since there were no AERONET measurements there at the time of the study). Using ground-measured AOD (including its wavelength dependence), we found mean biases of −7 W m^{-2} (PAY) and 3 W m^{-2} (PSA). For clear-sky measurement using MACC data, they found mean bias between −32 W m^{-2} and 2 W m^{-2}, the latter being the bias for PAY, while we found mean biases of −24 W m^{-2} (PSA) and −15 W m^{-2} (PAY). They only give the RMSD median over all stations using hourly averages of ground measurements for the comparisons. We did not compute RMSD of hourly averages for clear-sky events. For all-sky events, they found mean bias between 0 W m^{-2} and 30 W m^{-2} (12 W m^{-2} at PAY), while we found mean biases between 8 W m^{-2} and 55 W m^{-2} (depending on the AOD input) at PSA and between −5 W m^{-2} and 47 W m^{-2} at PAY. The median RMSD they found was 69 W m^{-2}, while we found larger RMSD for hourly averages (of the order of 125 W m^{-2} to 145 W m^{-2}).

Perez et al. (2002) compared DNI and GHI estimates from a model using cloud information from the Geostationary Operational Environmental Satellite (GOES) satellites with hourly averages of ground measurements from 10 United States (US) stations, three of which are associated to BSRN or the US Atmospheric Radiation Measurement (ARM) programme. They found mean bias between −42 W m^{-2} and 36 W m^{-2}, while RMSD is between 116 W m^{-2} and 193 W m^{-2}. These differences are of the same order or larger than those we found (see paragraph above).

Other studies either analysed only GHI and we do not compare these to our results for brevity (Bright 2019; Damiani et al. 2018; Kosmopoulos et al. 2018) or studied agreement for time averages over periods longer than we used (daily or longer), precluding comparison with our results (Castelli et al. 2014; Federico et al. 2017; Mueller and Traeger-Chatterjee 2014; Porfirio and Ceballos 2017).

4. Conclusions

We performed a validation of HelioMont surface DNI estimates with ground-based measurements from two European sites. The HelioMont algorithm (Stöckli 2013) infers irradiance using data from the Meteosat Second Generation SEVIRI instrument as primary source of information on clouds, while other influential input parameters are provided by models or reanalysis. The first validation site is the Plataforma Solar de Almería, a solar power research facility in Southern Spain. The PSA hosts several pyrheliometers mounted

on sun trackers providing high-quality DNI measurements over an area of about 1 km^2, the scale of the MSG/SEVIRI pixel resolution. This dataset is thus particularly well suited for our validation. The second site is the Swiss BSRN site of Payerne, including high accuracy DNI measurements. It does not host multiple pyrheliometers, but is characterized by a cloud coverage much more frequent than at PSA and allows verifying that the results obtained at PSA are not specific to its arid conditions.

Our analysis shows the importance of separately evaluating the quality of the determination of clear-sky irradiances, on one hand, and the treatment of the cloud effect by the HelioMont algorithm, on the other hand, (we use the cloud modification factor – CMF – to characterize this effect). This two-step validation mirrors the two-step process of the HelioMont algorithm.

The quality of the AOD input data is the main factor influencing the uncertainty of the clear-sky HelioMont DNI estimates. The HelioMont original AOD – a global climatology of AOD at 550 nm from Kinne (2008) – leads to negative mean biases of the order of 115 W m^{-2} to 145 W m^{-2}. Using the CAMS global AOD dataset still produces negative biases but reduced to 15 W m^{-2} to 25 W m^{-2} (2% to 3%). Around this bias, there is a dispersion of ±12% for PSA and ±15% for PAY. These ranges are much larger than the mean bias and include more than 90% of the data. They can thus be considered as a measure of expanded uncertainty, and such accuracy is already satisfactory for many applications. Finally, using measured AOD as input for HelioMont leads to negligible mean biases and a spread of ±6.5% at PSA and ±5% at PAY, which can also be considered as expanded uncertainty. These results are similar to those of Greuell, Meirink, and Wang (2013) who also analysed clear-sky DNI using equivalent AOD input schemes. Since stations measuring AOD are spatially scarce, AOD measurement cannot be used for generating DNI datasets of large spatial extent; but such uncertainty should be seen as a lower limit that HelioMont could reach in the estimation of clear-sky DNI, and enhancing the accuracy of global AOD datasets would be the key to such improvement. Applying the same analysis to GHI leads to similar conclusions, except that the uncertainties are lower for GHI estimates (CAMS-AOD HelioMont clear-sky GHI uncertainty is ±6% at both PSA and PAY, while measured AOD HelioMont clear-sky GHI uncertainty is ±4% at PSA and ±3% at PAY).

For all-sky events, differences between HelioMont estimates and ground-based measurements result from a combination of the inadequacies in the clear-sky estimation and in the cloud effect treatment, which are difficult to disentangle. At PSA, the mean biases are between about 8 W m^{-2} and 55 W m^{-2} (depending on the AOD input), while the RMSD is between about 185 W m^{-2} and 195 W m^{-2}. Similar results are obtained at PAY with mean biases between about −5 W m^{-2} and 45 W m^{-2} and RMSD between about 175 W m^{-2} and 185 W m^{-2}. These results are obtained by comparing 15 minute HelioMont estimates with 1 minute measurements taken at the time closest to SEVIRI scan. Comparisons using 15- or 60-minute averages of ground-based measurements have negligible effect on mean biases but decreases RMSD by about 15 W m^{-2} to 20 W m^{-2} (15 minutes) and 50 W m^{-2} (1 hour). In general, hourly averaging seems optimal when comparing point measurements with satellite estimates valid for areas of the order of the SEVIRI pixel resolution. Other studies that validated DNI estimates using a method similar to ours found mean biases and RMSD of the same order of magnitude. Two studies found RMSD slightly larger than ours (Eissa et al. 2015; Perez et al. 2002), while two other found RMSD smaller than ours (Amillo, Huld and Müller, 2014; Greuell, Meirink, and Wang 2013), but the inclusion of nigh-time data in the analysis of Amillo, Huld

and Müller (2014) probably significantly reduced the RMSD. It should be noted that in our analysis the all-sky mean biases are smallest when using the original Kinne (2008) AOD climatology. However, it is a misleading result due to error compensation as mentioned in the next paragraph.

In addition to the traditional validation method based on mean biases and RMSD, we also use a validation CMF derived from ground-based data (the ratio between the theoretical HelioMont clear-sky estimate and the ground-based measurement). This gives us more insight into event-by-event (or scatterplot) agreement between the tested HelioMont estimates and the ground-measured reference irradiances ('event' is here defined as instantaneous comparison in time or comparison of short-term averages: 15 minute or 1 hour). The CMF validation method first allows evaluating the general quality of the cloud treatment by HelioMont: the correlation between the HelioMont CMF and the validation CMF is good (Pearson's correlation coefficient r between 0.79 and 0.92) and the RMSD is typically between 0.18 and 0.24 for a quantity ranging from 0 to about 1. More importantly, the CMF analysis of event-by-event agreement allows identifying HelioMont weaknesses that are difficult to detect with aggregated distribution statistics. It clearly shows that HelioMont produces a certain number of low – *but non-zero* – CMF for which the corresponding ground-based validation CMF is zero or near-zero. This leads to an underestimation of the number of near-zero DNI cases. Similarly, a significant number of cases where the HelioMont CMF is near 1, but the validation CMF is lower are identified. This is consistent with thin clouds not detected using the MSG/SEVIRI data. We were unable to identify such cases before using the CMF validation technique. Such a method is less prone to be affected by error compensation. For instance, error compensation would in this case misleadingly lead to classifying the HelioMont all-sky estimate using the AOD Kinne climatology as having mean bias and RMSD with respect to ground-based DNI measurements that are smaller (mean bias) or comparable (RMSD) than those for estimates based on CAMS or measured AOD.

Given the difficulty of accurately predicting the effect of clouds on radiation, the treatment of the cloud effect by HelioMont is satisfactory when considering agreement for short-term temporal averages (e.g. 1 hour). However, with RMSD of the order of 0.2 for a quantity between 0 and 1, this is a much larger source of uncertainty than the clear-sky part of the algorithm for the two investigated sites. Solving the systematic effects we identified (underestimation of the number of near-zero DNI or overestimation of the number of clear-sky cases) may lead to substantial improvement.

Acknowledgements

The data used for this study are available upon request from the corresponding author. This work was partially funded by and conducted in the framework of project Direct Normal Irradiance Nowcasting methods for optimized operation of concentrating solar technologies (DNICast). DNICast funding from the European Union's Seventh Programme for research, technological development and demonstration was obtained under grant agreement No 608623. We thank ACTRIS, AERONET, and the scientists of the AERONET stations Málaga and Granada for providing data for this study and for the help with the operation and calibration of the sun photometer at PSA. We would like to acknowledge the interesting comments and suggestions from an anonymous reviewer that allowed us improving our manuscript.

Disclosure statement

No potential conflict of interest was reported by the authors.

Funding

This work was supported by the FP7 Energy [608623].

ORCID

Laurent Vuilleumier http://orcid.org/0000-0003-0222-2566
Angela Meyer http://orcid.org/0000-0003-4120-3827

References

AERONET 2020. "AErosol RObotic NETwork Web Site." National Aeronautics and Space Administration, USA. Accessed March 19 2020. https://aeronet.gsfc.nasa.gov/new_web/V3/climo_new/LEV20/Tabernas_PSA-DLR_500_interpolated.html

Amillo, A. G., T. Huld, and R. Müller. 2014. "A New Database of Global and Direct Solar Radiation Using the Eastern Meteosat Satellite, Models and Validation." *Remote Sensing* 6: 8165–8189. doi:10.3390/rs6098165.

Bellouin, N., J. Quaas, -J.-J. Morcrette, and O. Boucher. 2013. "Estimates of Aerosol Radiative Forcing from the MACC Re-analysis." *Atmospheric Chemistry and Physics* 13: 2045–2062. doi:10.5194/acp-13-2045-2013.

Berrisford, P., D. Dee, K. Fielding, M. Fuentes, P. Kallberg, S. Kobayashi, and S. Uppala. 2009. "The ERA-interim Archive Version 1.0." *ERA Report Series 1, ECMWF*. Reading, United Kingdom: European Centre for Medium Range Weather Forecasts.

Blanc, P., B. Espinar, N. Geuder, C. Gueymard, R. Meyer, R. Pitz-Paal, B. Reinhardt, et al. 2014. "Direct Normal Irradiance Related Definitions and Applications: The Circumsolar Issue." *Solar Energy* 110: 561–577. doi:10.1016/j.solener.2014.10.001.

Bright, J. M. 2019. "Solcast: Validation of a Satellite-derived Solar Irradiance Dataset." *Solar Energy* 189: 435–449. doi:10.1016/j.solener.2019.07.086.

Cano, D., J. Monget, M. Albuisson, H. Guillard, N. Regas, and L. Wald. 1986. "A Method for the Determination of the Global Solar Radiation from Meteorological Satellite Data." *Solar Energy* 37: 31–39. doi:10.1016/0038-092X(86)90104-0.

Castelli, M., R. Stöckli, D. Zardi, A. Tetzlaff, J. E. Wagner, G. Belluardo, M. Zebisch, and M. Petitta. 2014. "The Heliomont Method for Assessing Solar Irradiance over Complex Terrain: Validation and Improvements." *Remote Sensing of Environment* 152: 603–613. doi:10.1016/j.rse.2014.07.018.

Damiani, A., H. Irie, T. Horio, T. Takamura, P. Khatri, H. Takenaka, T. Nagao, T. Y. Nakajima, and R. R. Cordero. 2018. "Evaluation of Himawari-8 Surface Downwelling Solar Radiation by Ground-based Measurements." *Atmospheric Measurement Techniques* 11: 2501–2521. doi:10.5194/amt-11-2501-2018.

Dee, D. P., and S. Uppala. 2009. "Variational Bias Correction of Satellite Radiance Data in the ERA-Interim Reanalysis." *Quarterly Journal of the Royal Meteorological Society* 135: 1830–1841. doi:10.1002/qj.493.

DNICast FP7, 2020. "European Commission Seventh Framework Programme." *DNICast web page*. Accessed May 08 2020. https://cordis.europa.eu/project/id/608623/fr

Eissa, Y., M. Korany, Y. Aoun, M. Boraiy, M. M. Abdel-Wahab, S. C. Alfaro, P. Blanc, et al. 2015. "Validation of the Surface Downwelling Solar Irradiance Estimates of the HelioClim-3 Database in Egypt." *Remote Sensing* 7 :9269–9291. doi:10.3390/rs70709269.

Eskes, H., V. Huijnen, A. Arola, A. Benedictow, A.-M. Blechschmidt, E. Botek, O. Boucher, et al. 2015. "Validation of Reactive Gases and Aerosols in the MACC Global Analysis and Forecast System." *Geoscientific Model Development* 8 :3523–3543. doi:10.5194/gmd-8-3523-2015.

Federico, S., R. C. Torcasio, P. Sanò, D. Casella, M. Campanelli, J. F. Meirink, P. Wang, S. Vergari, H. Diémoz, and S. Dietrich. 2017. "Comparison of Hourly Surface Downwelling Solar Radiation Estimated from MSG-SEVIRI and Forecast by the RAMS Model with Pyranometers over Italy." *Atmospheric Measurement Techniques* 10: 2337–2352. doi:10.5194/amt-10-2337–2017.

Filonchyk, M., V. Hurynovich, H. Yan, L. Zhou, and A. Gusev. 2019. "Climatology of Aerosol Optical Depth over Eastern Europe Based on 19 Years (2000–2018) MODIS TERRA Data." *International Journal of Climatology* 1–19. doi:10.1002/joc.6412.

Geuder, N., F. Wolfertstetter, S. Wilbert, D. Schüler, R. Affolter, B. Kraas, E. Lüpfert, and B. Espinar. 2015. "Screening and Flagging of Solar Irradiation and Ancillary Meteorological Data." *Energy Procedia* 69: 1989–1998. doi:10.1016/j.egypro.2015.03.205.

Greuell, W., J. F. Meirink, and P. Wang. 2013. "Retrieval and Validation of Global, Direct, and Diffuse Irradiance Derived from SEVIRI Satellite Observations." *Journal of Geophysical Research: Atmospheres* 118: 2340–2361. doi:10.1002/jgrd.50194.

Holben, B. N., T. F. Eck, I. Slutsker, D. Tanre, J. P. Buis, A. Setzer, E. Vermote, J. A. Reagan, Y. J. Kaufman, and T. Nakajima. 1998. "AERONET – A Federated Instrument Network and Data Archive for Aerosol Characterization." *Remote Sensing of Environment* 66 (1): 1–16. doi:10.1016/S0034-4257(98)00031-5.

Huang, G., X. Li, C. Huang, S. Liu, Y. Ma, and H. Chen. 2016. "Representativeness Errors of Point-Scale Ground-Based Solar Radiation Measurements in the Validation of Remote Sensing Products." *Remote Sensing of Environment* 181: 198–206. doi:10.1016/j.rse.2016.04.001.

Inness, A., F. Baier, A. Benedetti, I. Bouarar, S. Chabrillat, H. Clark, C. Clerbaux, et al. 2013. "The MACC Reanalysis: An 8 Year Data Set of Atmospheric Composition." *Atmospheric Chemistry and Physics* 13 :4073–4109. doi:10.5194/acp-13-4073-2013.

Kinne, S. 2008. "Climatologies of Cloud Related Aerosols: Particle Number and Size." In *Clouds in the Perturbed Climate System*, Edited by J. Heintzenberg and R. J. Charlson, pp. 37-57. Cambridge, Massachusetts (USA): MIT Press.

Kinne, S., M. Schulz, C. Textor, S. Guibert, Y. Balkanski, S. E. Bauer, T. Berntsen, et al. 2006. "An AeroCom Initial Assessment – Optical Properties in Aerosol Component Modules of Global Models." *Atmospheric Chemistry and Physics* 6 :1815–1834. doi:10.5194/acp-6-1815-2006.

Kosmopoulos, P. G., S. Kazadzis, M. Taylor, P. I. Raptis, I. Keramitsoglou, C. Kiranoudis, and A. F. Bais. 2018. "Assessment of Surface Solar Irradiance Derived from Real-time Modelling Techniques and Verification with Ground-based Measurements." *Atmospheric Measurement Techniques* 11: 907–924. doi:10.5194/amt-11-907-2018.

Li, Z., M. C. Cribb, F.-L. Chang, A. Trishchenko, and Y. Luo. 2005. "Natural Variability and Sampling Errors in Solar Radiation Measurements for Model Validation over the Atmospheric Radiation Measurement Southern Great Plains Region." *Journal of Geophysical Research: Atmospheres* 110: D15S19. doi:10.1029/2004JD005028.

Long, C. N., and T. Ackermann. 2000. "Identification of Clear Skies from Broadband Pyranometer Measurements and Calculation of Downwelling Shortwave Cloud Effects." *Journal of Geophysical Research: Atmospheres* 105: 15609–15626. doi:10.1029/2000JD900077.

Long, C. N., and E. G. Dutton. 2010. "BSRN Global Network Recommended QC Tests, Bremerhaven, PANGAEA." Technical Report. http://epic.awi.de/30083/1/BSRN_recommended_QC_tests_V2.pdf

Mayer, B., and A. Kylling. 2005. "Technical Note: The libRadtran Software Package for Radiative Transfer Calculations – Description and Examples of Use." *Atmospheric Chemistry and Physics* 5 (7): 1855–1877. doi:10.5194/acp-5-1855-2005.

Moeser, W., and E. Raschke. 1984. "Incident Solar Radiation over Europe Estimated from Meteosat Data." *Journal of Applied Meteorology and Climatology* 23: 166–179. doi:10.1175/1520-0450(1984)023<0166:ISROEE>2.0.CO;2.

Mueller, R., U. Pfeifroth, and C. Traeger-Chatterjee. 2015. "Towards Optimal Aerosol Information for the Retrieval of Solar Surface Radiation Using Heliosat." *Atmosphere* 6: 863–878. doi:10.3390/atmos6070863.

Mueller, R., and C. Traeger-Chatterjee. 2014. "Brief Accuracy Assessment of Aerosol Climatologies for the Retrieval of Solar Surface Radiation." *Atmosphere* 5: 959–972. doi:10.3390/atmos5040959.

Mueller, R. W., K. F. Dagestad, P. Ineichen, M. Schroedter-Homscheidt, S. Cros, D. Dumortier, R. Kuhlemann, et al. 2004. "Rethinking Satellite-based Solar Irradiance Modelling – The SOLIS Clear-sky Module." *Remote Sensing of Environment* 91 :160–174. doi:10.1016/j.rse.2004.02.009.

Mueller, R. W., C. Matsoukas, A. Gratzki, H. D. Behr, and R. Hollmann. 2009. "The CM-SAF Operational Scheme for the Satellite Based Retrieval of Solar Surface Irradiance — A LUT Based Eigenvector Hybrid Approach." *Remote Sensing of Environment* 113: 1012–1024. doi:10.1016/j.rse.2009.01.012.

Nouri, B., S. Wilbert, P. Kuhn, N. Hanrieder, M. Schroedter-Homscheidt, A. Kazantzidis, L. Zarzalejo, et al. 2019. "Real-Time Uncertainty Specification of All Sky Imager Derived Irradiance Nowcasts." *Remote Sensing* 11 (9): 1059. doi:10.3390/rs11091059.

Ohmura, A., E. G. Dutton, B. Forgan, C. Fröhlich, H. Gilgen, H. Hegner, A. Heimo, et al. 1998. "Baseline Surface Radiation Network (BSRN/WCRP): New Precision Radiometry for Climate Research." *Bulletin of the American Meteorological Society* 79 :2115–2136. doi:10.1175/1520-0477(1998)079<2115:BSRNBW>2.0.CO;2.

Perez, R., P. Ineichen, K. Moore, M. Kmiecik, C. Chain, R. George, and F. Vignola. 2002. "A New Operational Model for Satellite-derived Irradiances: Description and Validation." *Solar Energy* 73: 307–317. doi:10.1016/S0038-092X(02)00122-6.

Porfirio, A. C. S., and J. C. Ceballos. 2017. "A Method for Estimating Direct Normal Irradiation from GOES Geostationary Satellite Imagery: Validation and Application over Northeast Brazil." *Solar Energy* 155: 178–190. doi:10.1016/j.solener.2017.05.096.

Posselt, R., R. Mueller, J. Trentmann, R. Stockli, and M. A. Liniger. 2014. "A Surface Radiation Climatology across Two Meteosat Satellite Generations." *Remote Sensing of Environment* 142: 103–110. doi:10.1016/j.rse.2013.11.007.

Posselt, R., R. W. Müller, R. Stöckli, and J. Trentmann. 2012. "Remote Sensing of Solar Surface Radiation for Climate Monitoring – The CM-SAF Retrieval in International Comparison." *Remote Sensing of Environment* 118: 186–198. doi:10.1016/j.rse.2011.11.016.

Rizza, U., E. Mancinelli, M. Morichetti, G. Passerini, and S. Virgili. 2019. "Aerosol Optical Depth of the Main Aerosol Species over Italian Cities Based on the NASA/MERRA-2 Model Reanalysis." *Atmosphere* 10: 709. doi:10.3390/atmos10110709.

Ruckstuhl, C., R. Philipona, K. Behrens, M. Collaud Coen, B. Dürr, A. Heimo, C. Mätzler, et al. 2008. "Aerosol and Cloud Effects on Solar Brightening and the Recent Rapid Warming." *Geophysical Research Letters* 35 :L12708. doi:10.1029/2008GL034228.

Schroedter-Homscheidt, M., and S. Wilbert. 2017. "8 - Methods to Provide Meteorological Forecasts for Optimum CSP System Operations." In *The Performance of Concentrated Solar Power (CSP) Systems*, edited by P. Heller, 253–281, Woodhead Publishing, Duxford, United Kingdom.

Slingo, A., T. P. Ackerman, R. P. Allan, E. I. Kassianov, S. A. McFarlane, G. J. Robinson, J. C. Barnard, et al. 2006. "Observations of the Impact of a Major Saharan Dust Storm on the Atmospheric Radiation Balance." *Geophysical Research Letters* 33 :L24817. doi:10.1029/2006GL027869.

Stöckli, R. 2013. "The HelioMont Surface Solar Radiation Processing." *Scientific Report MeteoSwiss*, **93**, Zurich: Federal Office of Meteorology and Climatology MeteoSwiss.

Vuilleumier, L., M. Hauser, C. Félix, F. Vignola, P. Blanc, A. Kazantzidis, and B. Calpini. 2014. "Accuracy of Ground Surface Broadband Shortwave Radiation Monitoring." *Journal of Geophysical Research: Atmospheres* 119. doi:10.1002/2014JD022335.

Wilbert, S., B. Reinhardt, J. DeVore, M. Röger, R. Pitz-Paal, C. Gueymard, and R. Buras. 2013. "Measurement of Solar Radiance Profiles with the Sun and Aureole Measurement System." *Journal of Solar Energy Engineering* 135 (4): 041002. doi:10.1115/1.4024244.

Zou, L., S. Griessbach, L. Hoffmann, B. Gong, and L. Wang. 2020. "Revisiting Global Satellite Observations of Stratospheric Cirrus Clouds." *Atmospheric Chemistry and Physics Discussions* in review. doi:10.5194/acp-2020-304.